Energy & Environmental Science

High-Throughput Oxygen Chemical Potential Engineering of Perovskite Oxides for Chemical Looping Applications

Journal:	*Energy & Environmental Science*
Manuscript ID	EE-ART-09-2021-002889.R2
Article Type:	Paper
Date Submitted by the Author:	17-Feb-2022
Complete List of Authors:	Wang, Xijun; North Carolina State University, Chemical and Biomolecular Engineering Gao, Yunfei; North Carolina State University, Chemical Engineering Krzystowczyk, Emily; North Carolina State University, Chemical Engineering Iftikhar, Sherafghan; North Carolina State University Dou, Jian; North Carolina State University, Chemical Engineering Cai, Runxia; North Carolina State University Wang, Haiying; Northeast Petroleum University Ruan, Chongyan; North Carolina State University, Chemical and Biomolecular Engineering Ye, Sheng; University of Science and Technology of China Li, Fanxing; North Carolina State University, Chemical Engineering

ARTICLE

High-Throughput Oxygen Chemical Potential Engineering of Perovskite Oxides for Chemical Looping Applications

Received 00th January 20xx,
Accepted 00th January 20xx

DOI: 10.1039/x0xx00000x

Xijun Wang,‡[a] Yunfei Gao,‡[a] Emily Krzystowczyk,‡[a] Sherafghan Iftikhar,[a] Jian Dou,[a] Runxia Cai,[a] Haiying Wang,[a,b] Chongyan Ruan,[a] Sheng Ye,[c] Fanxing Li,*[a]

Chemical looping (CL) represents a versatile, emerging strategy for sustainable chemical and energy conversion. Designing metal oxide oxygen carriers with suitable redox properties remains one of the most critical challenges to CL due to the considerably different thermodynamic property requirements for different applications. Taking $SrFeO_{3-\delta}$ as a base-structure, this study seeks to rationally substitute its A- and/or B-site cations to tailor the equilibrium oxygen partial pressure over 20 orders of magnitude. 2,401 $Sr_xA_{1-x}Fe_yB_{1-y}O_{3-\delta}$ perovskite-phase structures were investigated using high-throughput density functional theory (DFT) and 227,273 high-entropy perovskites were screened via machine learning (ML). This significantly expands the materials design space. While most of the compositions predicted are new and nonobvious, 19 previously reported oxygen carriers, with excellent redox properties, were correctly identified by the algorithm. Moreover, we experimentally demonstrated 15 new oxygen carriers with superior redox performance. These results support the effectiveness of the high-throughput approaches for accelerated materials discovery.

Broader context

Due to their unique redox properties, perovskite oxides containing first-row transition metals have drawn substantial attention in the areas of chemical looping, catalysis, electrochemistry, energy storage, solar-thermal water and CO_2 splitting, and beyond. In these applications, designing mixed oxides with tailored redox properties is of critical importance. Despite the tremendous recent progress, development of mixed oxides still primarily relies on heuristic-based approaches. Building upon recent advances in computations, this study aims at significantly expanding the design space of perovskite oxides with tailored redox properties via high throughput DFT calculations supplemented with machine learning and verified with extensive experimental data. The effectiveness of this approach is highlighted by many of the predicted perovskites outperforming the previous benchmark by a factor of >2. Although two chemical looping applications are used as examples, this approach can be generalized for various energy, chemical, and environmental related applications, thus opening new avenues for rational design of high-performance oxides.

1. Introduction

As an emerging strategy toward clean, efficient, and cost-effective energy and chemical conversion, chemical looping (CL) has drawn substantial attention in various important applications such as air separation,[1-4] indirect combustion for CO_2 capture,[5-7] solar thermal water or CO_2 splitting,[8-10] and selective oxidation for chemical production.[11-16] The CL concept involves decoupling an overall reaction into multiple reduction and oxidization sub-reactions, whereby an intermediate, also known as an oxygen carrier or a redox catalyst, facilitates such sub-reactions by releasing or replenishing oxygen under temperature and/or oxygen partial pressure (P_{O2}) swings (Fig. 1a).[13,17-19] Therefore, the properties of the oxygen carriers, often composed of transition metal oxides, play a critical role towards the overall performances of a CL process. Despite of the tremendous efforts in oxygen carrier development, which has resulted in more than 2,000 journal articles, development and optimization of oxygen carriers still rely primarily on heuristics and trial-and-error. Meanwhile, the design space for oxygen carriers have significantly expanded from supported monometallic transition metal oxide[20-22] to various families of mixed oxides.[12,23-26] Since possible compositions of mixed oxides are practically infinite, effective computational tools that can narrow down the material design space for oxygen carrier development and optimization are highly desirable.

[a] Department of Chemical and Biomolecular Engineering, North Carolina State University, Raleigh, North Carolina 27606, United States. Email: fli5@ncsu.edu
[b] College of Chemistry & Chemical Engineering, Northeast Petroleum University, Daqing, 163318, P. R. China
[c] Hefei National Laboratory for Physical Sciences at the Microscale, Collaborative Innovation Center of Chemistry for Energy Materials, CAS Center for Excellence in Nanoscience, School of Chemistry and Materials Science, University of Science and Technology of China, Hefei, Anhui 230026, P. R. China

† Electronic Supplementary Information (ESI) available. See DOI: 10.1039/x0xx00000x

‡ These authors equally contributed to this work.

ARTICLE

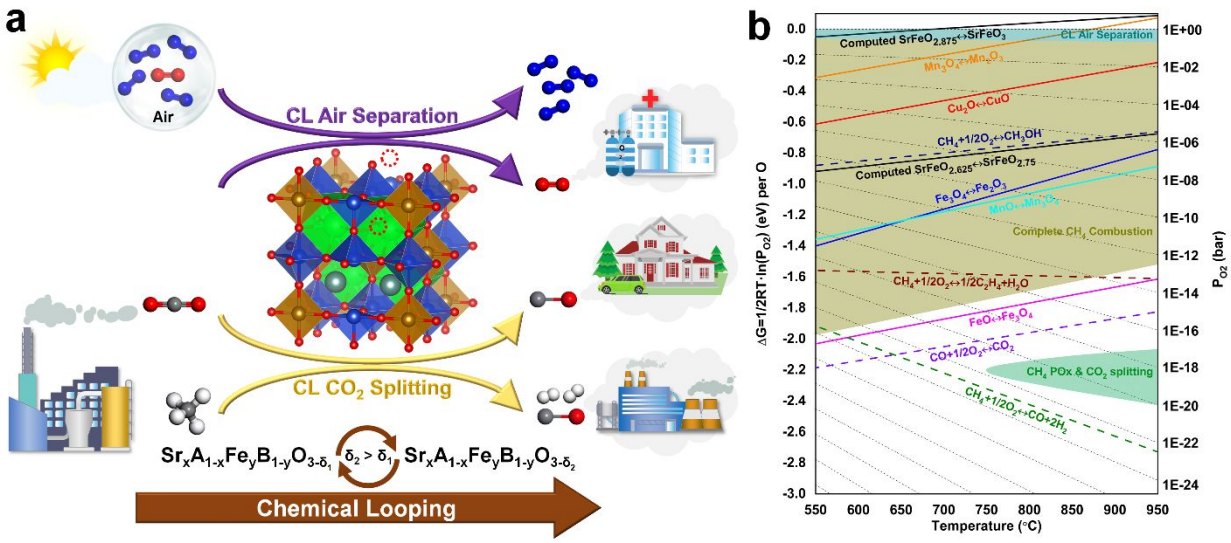

Fig. 1 Chemical looping strategy. (a) Schematic illustration and potential applications. (b) Ellingham diagram depicting the correspondence between oxygen carrier redox properties and applications.

Oxygen carrier optimization requires comprehensive consideration of redox kinetics,[13,27-30] oxygen capacity,[31] redox cycling stability,[32] cost, environmental impact, and surface catalytic properties[13,33,34] when applied towards chemical production. The complexity of these intertwined factors makes it impractical for a comprehensive investigation from a computational standpoint, especially considering the dynamic nature of chemical looping reactions.[16,35] However, we note that the redox thermodynamic properties of the oxygen carriers, quantified as equilibrium oxygen chemical potential (μ_{O2}) or partial pressure (P_{O2}),[33,36,37] represent the utmost important parameter and a prerequisite for oxygen carrier selection. Depending on the applications, the required P_{O2} may vary by up to 20 orders of magnitudes (Fig. 1b).[33] As one would anticipate, high P_{O2} would promote oxygen donation while low P_{O2} would favor oxygen storage or replenishment,[13,38] making the equilibrium oxygen chemical potential a promising descriptor to down-select oxide candidates for oxygen carrier design.

First-principles density function theory (DFT) calculations have shown advantages in computing redox thermodynamics for oxygen carriers.[17,38-41] Recent studies have demonstrated the correspondence between the computed oxygen vacancy formation energies and the experimental PO_2 swings.[2,38,39,42] To this end, a number of DFT-driven high-throughput studies have been performed:[2,44,45] Lau et al. reported an in-silico study calculating the theoretical redox equilibria for thousands of oxides and simulated their performance for chemical looping combustion (CLC);[2] Vieten et al. calculated the enthalpies for the reduction of 240 perovskites to their brownmillerite phases and proposed an empirical model to pre-select materials for thermochemical water and CO_2-splitting;[42] Singstock et al. applied a DFT-computed descriptor to identify over 1,300 promising active materials for CLC and chemical looping sulfur oxidation (CLSO).[44] These studies have demonstrate excellent effectiveness for material screening. However, they are still subject to one or more of the following limitations: 1) The oxide model structures were generally simulated with small unit cells, making it difficult to determine the effects of oxygen vacancy concentration, which dynamically changes over the course of the redox reactions; 2) Thermodynamic properties were generally calculated using a defect-free model as the starting point, but the actual oxygen carriers rarely stay near a pristine state; 3) The various possible vacancy and substitution site combinations were not comprehensively considered. The accuracy of the DFT calculation results can be affected by the functional/basis-sets and some parameters settings like the U_{eff} values. These limitations can impact the accuracy and applicability of the models especially for applications with small target PO_2 ranges such as CL air separation (CLAS) (Fig. 1b). Therefore, a more comprehensive simulation scheme closer to real world conditions is highly desired. In addition, advanced data-driven techniques such as ML, which have been successfully applied to assist materials design,[46-51] have rarely been used for CL applications, with the exception of one study

investigating Mn based oxygen carriers based on experimental performance and characterization of 19 Mn-containing ores.[52]

Perovskite structured strontium ferrite ($SrFeO_{3-\delta}$) has been widely investigated for CLAS[2,19,38,53] and CL with oxygen uncoupling (CLOU)[54,55] due to its outstanding oxygen release and uptake capabilities.[56-62] However, unless reduced well below $SrFeO_{2.5}$, $SrFeO_{3-\delta}$ cannot be applied for reactions that require much lower P_{O2} such as CO_2/H_2O splitting.[63] Substitution of the A- and/or B-site of $SrFeO_3$ was shown to be effective toward fine-tuning its redox properties.[38,39,64-67] For instance, A-site doping with La[64] or Ca[65], B-site doping with Cu[66] or Mn[67], and A/B-site co-doping with La/Co[68,69] or Ca/Co[53,70] have improved the performance of $SrFeO_3$ based oxygen carriers for CLAS. These studies confirm that cation substitution can tailor the partial molar enthalpy (ΔH) and the entropy (ΔS) for redox reactions. However, finding the optimal doping elements and concentrations for specific applications still rely heavily on trial-and-error. Moreover, further expanding the redox property range of doped $SrFeO_{3-\delta}$ towards ultra-low P_{O2} applications such as CO_2 splitting is highly desirable.

Herein, we demonstrate that the oxygen chemical potentials of A- and/or B-site substituted $SrFeO_{3-\delta}$ perovskites can be rationally engineered for a wide range of CL applications. Specifically, DFT based high throughput calculations, with procedures depicted in Fig. 2a, were applied to investigate $Sr_xA_{1-x}Fe_yB_{1-y}O_{3-\delta}$ perovskites with 2401 distinct cation compositions. DFT calculated ΔGs at various oxygen non-stoichiometries (δs) and temperatures were used to screen out promising oxygen carrier materials for CLAS and CL based CO_2 splitting. The effectiveness of the DFT based high throughput screening is supported by 21 literature reported oxygen carriers and 15 new carrier compositions prepared and tested in the current study. Furthermore, the DFT results were used to develop a machine learning model to predict the ΔGs of 227,273 $Sr_x(A/A')_{1-x}Fe_y(B/B')_{1-y}O_{3-\delta}$ high-entropy perovskites containing 5 cation elements.[71] The machine learning protocol, as illustrated in Fig. 2b, contains the following steps:[72] (1) Data preparation, which includes data collection, normalization, and splitting the data into training and test datasets, as well as defining the input features; (2) Model selection, which involves selecting ML algorithms for the studied datasets based on the trade-off between time-consumption and accuracy; (3) Training model, referring to training the hyperparameters within the framework of the selected algorithm using the training sets to improve the prediction of the ML model; (4) Model evaluation, which entails testing the ML model against an unused dataset (test set) to evaluate its performances; (5) Predict the values of the new targets (ΔGs) for new perovskite compositions, followed by additional DFT and/or experimental verifications. The accuracy of the ML model was validated by additional DFT calculations and experiments. These findings not only significantly expand the materials design space for CL applications but also provide new insights and theoretical guidance for oxygen carrier optimization.

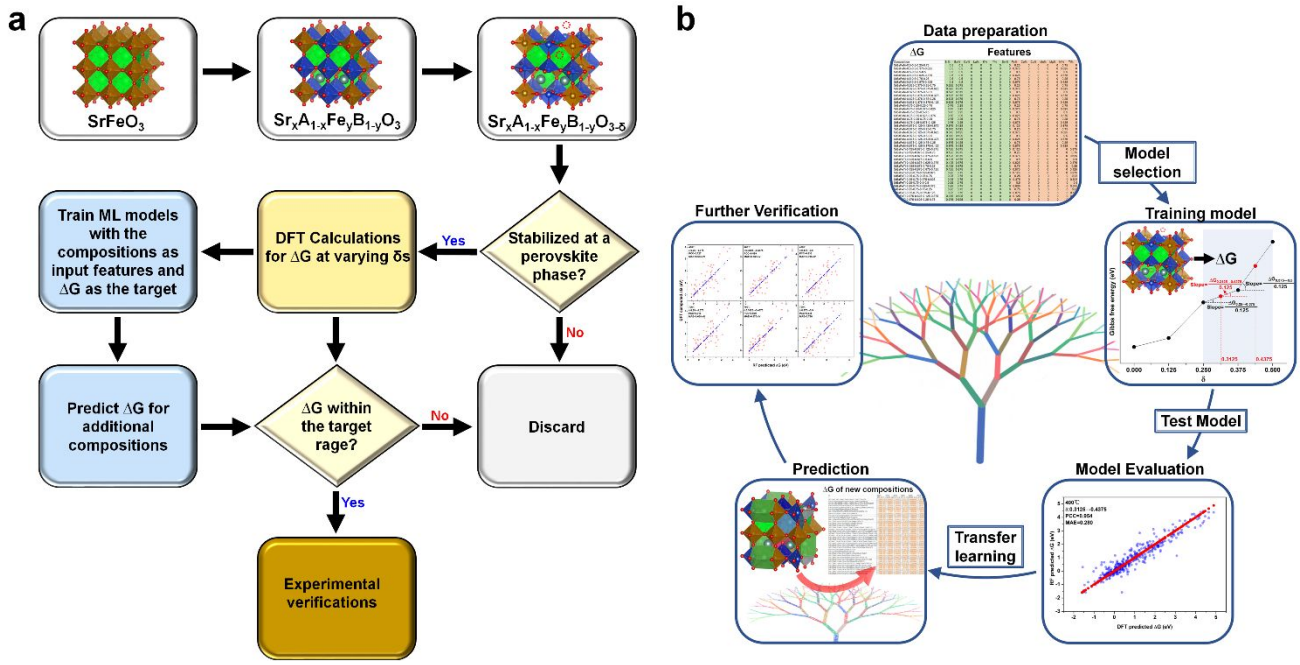

Fig. 2 Flowcharts for high throughput materials screening. (a) DFT model construction, high-throughput calculations, and materials screening. (b) ML steps for the training, evaluation, and prediction of perovskite datasets.

2. Results and Discussion

2.1 Preliminary screening based on structural stability

The $Sr_xA_{1-x}Fe_yB_{1-y}O_3$ perovskite models were constructed by substituting A- and/or B-site cations in $SrFeO_3$, where A-site cations are typically consisted of alkaline earth, alkali or rare

earth metals and B-site cations are usually transition metals. Table 1 summarizes the dopant types and concentrations investigated in this study. By exhausting all possible combinations of A- and/or B-site dopants in the selected cation network, 2401 perovskite models were constructed. Since some of these compositions may not form a stable perovskite phase, pre-screening steps were performed. Firstly, 168 compositions whose total valence cannot be zero were excluded (see Section 2 in Supplemental Information), most of them contain large proportions (> 50%) of Mg on the B-site.

Table 1 A- and B-site dopant elements, x, y, and δ in $Sr_xA_{1-x}Fe_yB_{1-y}O_{3-\delta}$ investigated

A-site dopants	*Ca, K, Y, Ba, La, Sm*
B-site dopants	Co, Cu, Mn, Mg, Ni, Ti
x	0, 0.125, 0.25, 0.375, 0.5, 0.625, 0.75, 0.875, 1
y	0, 0.125, 0.25, 0.375, 0.5, 0.625, 0.75, 0.875, 1
δ	0, 0.125, 0.25, 0.375, 0.5,

Besides charge neutrality, the Goldschmidt tolerance factor ($\boldsymbol{t} = \frac{r_A + r_O}{\sqrt{2}(r_B + r_O)}$) is a frequently used empirical parameter to estimate the stabilities of perovskites.[40] In a recent study, Bartel *et al.* proposed a modified tolerance factor $\boldsymbol{\tau} = \frac{r_O}{r_B} - \boldsymbol{n_A}\left(\boldsymbol{n_A} - \frac{r_A/r_B}{\ln\left(r_A/r_B\right)}\right)$,[73] where $\boldsymbol{r_O}$, $\boldsymbol{r_A}$, $\boldsymbol{r_B}$ represent the radii of oxygen anion, and A- and B-site cations (Table S2). $\boldsymbol{n_A}$ and $\boldsymbol{n_B}$ are the oxidation states of A- and B-site cations, respectively. The modified tolerance factor (τ) carries more chemical information and exhibits better predictive ability than the classical Goldschmidt tolerance factor. Therefore, the modified tolerance factor, τ, was applied to estimate the stabilities of the perovskite structures (Fig. 3a). Direct estimation of τ in $Sr_xA_{1-x}Fe_yB_{1-y}O_{3-\delta}$ is challenging since the oxidation states and the ionic radii of Fe and other multi-valent B site cations are difficult to specify. This can be exemplified by $Sr_{0.5}^{2+}Y_{0.5}^{3+}Fe_{0.5}^{a+}Co_{0.5}^{b+}O_3^{2-}$, where we can easily determine a + b=7, but the exact values of a and b are unknown. This can affect the calculations of the average radius of B site cations. To accommodate the $Sr_xA_{1-x}Fe_yB_{1-y}O_{3-\delta}$ system, τ is expressed as a function of $\boldsymbol{\tau}(\boldsymbol{n_A},\boldsymbol{n_B},\boldsymbol{x},\boldsymbol{y},\boldsymbol{\delta})$ (see Supplemental Information Section 3 for detailed derivation). For a given composition with a B-site element that has multiple oxidation states, all the parameters are fixed except for $\boldsymbol{n_B}$, which should be between its lowest and highest oxidation states (Table S2). Therefore, $\boldsymbol{\tau}(\boldsymbol{n_A},\boldsymbol{n_B},\boldsymbol{x},\boldsymbol{y},\boldsymbol{\delta})$ should also be within a corresponding range. Since tolerance factor is used only as a preliminary screening step, a less stringent standard was adopted: a composition is considered to be feasible as long as its minimum $\boldsymbol{\tau}(\boldsymbol{n_A},\boldsymbol{n_B},\boldsymbol{x},\boldsymbol{y},\boldsymbol{\delta})$ value is lower than a threshold value of 4.3, instead of 4.18 originally proposed by Bartel *et al.*[73] This is value is used because there are stable perovskites whose τs are slightly higher than 4.18, as suggested by the same authors.[73]

ARTICLE

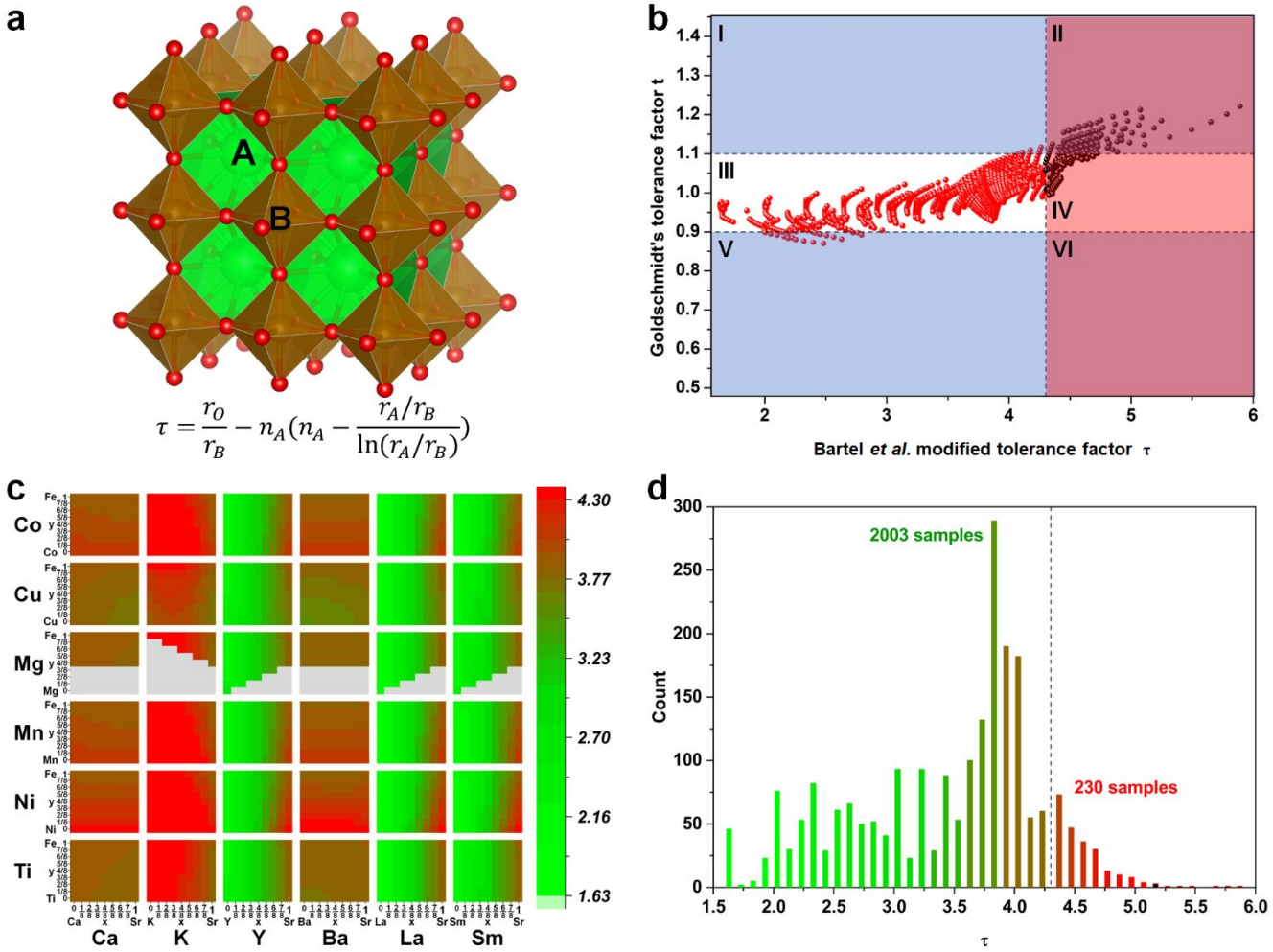

Fig. 3 Tolerance factor-based material screening. (a) Formula of the modified tolerance factor (τ) for ABO_3 perovskites. (b) Comparison of Goldschmidt's and the Bartel *et al.'s* modified tolerance factor for the 2401 $Sr_xA_{1-x}Fe_yB_{1-y}O_3$ samples considered. Candidates in panels III and IV are considered as stable perovskites according to Goldschmidt's rule and candidates in panels I, III and V are suitable candidates according to the modified tolerance factor τ. (c) Heatmap and (d) Frequency counts of the modified tolerance factors of the 2401 $Sr_xA_{1-x}Fe_yB_{1-y}O_3$ compositions considered. The grey areas refer to the 168 excluded compositions whose total valence cannot be balanced to zero.

Fig. 3b illustrates the correlation between the Goldschmidt's tolerance factor (*t*) and the modified tolerance factor (τ). Candidates in panels III and IV are considered as stable perovskites according to Goldschmidt's rule and candidates in panels I, III and V are suitable candidates according to the modified tolerance factor τ. Although the predictions largely overlap with each other, a main disagreement is seen on panel IV, where the classical criterion indicates that these samples would be stable perovskites. We note that most candidates in panel IV contain > 50% potassium at the A-sites, which tend to be unstable based on our experiences. This indicates that the modified tolerance factor is likely to be more accurate in predicting the stabilities of perovskites. Therefore, we relied on the modified tolerance factor for this pre-screening step. The candidates excluded either contain a large proportion of potassium at A-site (> 50%) or a large proportion of Ni at B-site with A being Ca or Ba (Fig. 3c). Of all the candidates considered, 230 were screened out, leaving 2,003 candidates for high-throughput calculations (Fig. 3d).

2.2 High throughput calculations of ΔG

The redox properties of oxygen carriers play a key role in CL processes. However, it is challenging to precisely describe the redox properties of oxygen carriers with simple yet accurate theoretical indicators. Although there are some successful case-studies using the initial vacancy formation energy (ΔE_V) of a perfect perovskite structure as a descriptor,[17,74,75] the initial ΔE_V alone, in most cases, does not correlate well with the experimental observations due to the following reasons: i) the oxygen carriers rarely start from a defect-free state under practical experimental conditions; ii) both vacancy concentration and ΔE_V change with oxygen partial pressure or temperature swings; iii) ΔE_V does not account for entropy changes, which can be very important especially at high temperatures. To address these limitations, Gibbs free energy changes (ΔGs) within specified δ ranges were used as the descriptor for the redox properties. The ΔG(δ) can be directly compared to the experimental P_{O2} and its effectiveness has been demonstrated in our previous theoretical and experimental works.[38,39] As illustrated in Fig. 4a, the $Sr_xA_{1-x}Fe_yB_{1-y}O_{3-\delta}$ oxygen carriers' redox thermodynamics can be described by their incremental Gibbs free energy as denoted by $\boldsymbol{\Delta G_{\delta_1\rightarrow\delta_2} = \Delta G_{\delta_2} - \Delta G_{\delta_1} + \left(\frac{\delta_2-\delta_1}{2}\right)\mu_{O_2}}$, where $\boldsymbol{\delta_1\rightarrow\delta_2}$ represent the change of δ value from δ_1 to δ_2. The slope of the δ vs. G curve ($\frac{\Delta G_{\delta_1\rightarrow\delta_2}}{\delta_2-\delta_1} \propto \boldsymbol{\Delta G_{\delta_1\rightarrow\delta_2}}$) thus describe the μ_{O2} (or P_{O2}) within a vacancy concentration range at a given temperature. They can in turn be used to determine the feasibility and capacity of oxygen uptake and release within a given P_{O2} and/or temperature swings. As one can anticipate, too large or too small $\boldsymbol{\Delta G_{\delta_1\rightarrow\delta_2}}$ will lead to less or over stable configurations. Therefore, a suitable $\boldsymbol{\Delta G_{\delta_1\rightarrow\delta_2}}$ within an optimal range over a large δ span would lead to a larger oxygen capacity. Previous experiments indicate that δ usually varies in the range of 0.25 ~ 0.5 in CL processes. It is also noted that every 0.125 change in δ correspond to roughly 1 wt% oxygen capacity. Therefore, we focused our study on the ΔG within a δ range of 0.25 and 0.5 with 0.125 increment, i.e. $\boldsymbol{\Delta G_{0.25\rightarrow0.375}}$ and $\boldsymbol{\Delta G_{0.375\rightarrow0.5}}$. as well as their linear interpolation $\boldsymbol{\Delta G_{0.3125\rightarrow0.4375}}$.

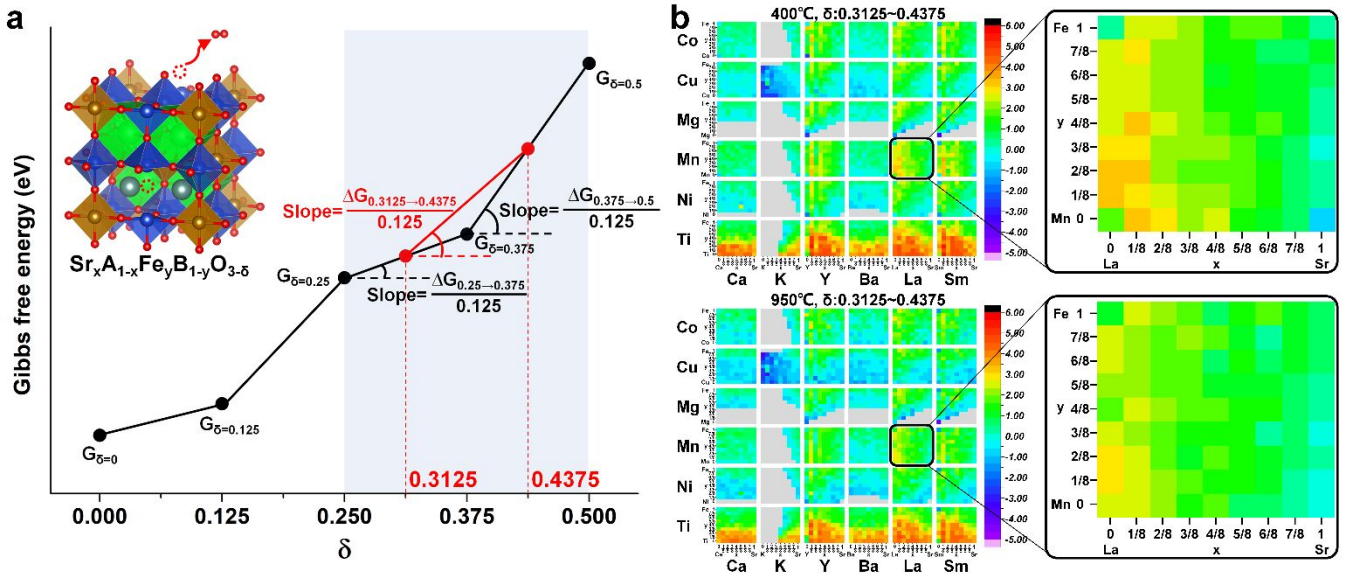

Fig. 4 ΔGs for oxygen vacancy formation. (a) Schematic of the slope of ΔG in different δ ranges, where ΔG can be directly correlated with P_{O2} by $\boldsymbol{\Delta G = -\frac{1}{2}RT\ln\frac{P_{O_2}}{P^0}}$. (b) ΔG of each doped species as δ changes from 0.3125 to 0.4375 at 400 and 950 °C. The grey areas refer to the 398 excluded unstable compositions.

Using ΔGs as the descriptor, high-throughput DFT calculations were carried out on the 2,003 $Sr_xA_{1-x}Fe_yB_{1-y}O_{3-\delta}$ candidates. It is noted that many perovskite structures undergo a disorder-order transition of lattice oxygen during the process of oxygen release, forming a brownmillerite structure at large δs (a perovskite phase tends to be maintained at very high operating temperatures). Such phase transition will have different effects on the calculations of ΔG for different materials. To account for this, both the energies of perovskite and brownmillerite structures were calculated for all the candidates with δ =0.5 and we used the lower value to calculate the corresponding ΔGs at 400 — 700 °C. For higher temperatures (800 — 950 °C), such transition was not considered since most of the materials should have disordered vacancies. Fig. S2 summarizes all the ΔG results at low (e.g. 400 °C) and high (e.g. 950 °C) temperatures. As will be demonstrated in Section 3.4, these results are very useful to guide the development of high-performance oxygen carriers for a variety of CL applications.

The computation results indicate that substitution of A- and/or B-site cation in $SrFeO_{3-\delta}$ can tune the redox ΔGs over very broad ranges (-6.15 eV ~ 6.70 eV at 400 °C and -6.69 eV ~ 6.14 eV at 950 °C). From the ΔG heatmap patterns, some general correlations between the dopant types, proportions and ΔGs can be captured. For instance, as exemplified by the **Δ**

$G_{0.3125\rightarrow0.4375}$ in Fig. 4b, the horizontal axis in each panel is the composition parameter x of Sr in $Sr_xA_{1-x}Fe_yB_{1-y}O_{3-\delta}$ and the vertical axis is the composition parameter y of Fe. It is clear that specific doping elements or combinations of co-doping elements can significantly affect the ΔG values. For instance, Ti-doping tends to increase the ΔGs, in some cases greater than 6 eV, while Cu-doping, especially Cu-K co-doping, significantly decreases the ΔGs. These findings can reduce the experimental trail-and-error for accelerated material discovery.

2.3 ML training and prediction of catalytic performances

The large datasets from high-throughput DFT allows us to perform further data analyses with ML to explore the correlations between the composition of perovskites and their ΔGs within the studied δ ranges. To select the appropriate ML model for our datasets, some test fittings were performed using a series of supervised learning algorithms. The studied algorithms include the family of linear models (linear fitting, and its regularized version Ridge[76] and Lasso[77]), support vector machines (SVM) with different kernel functions,[78] nearest neighbors,[79] Gaussian process,[80] and the decision trees[81] etc. Here, the proportion of each cation element of the 2003 perovskites are used as the input features (Fig. S3) and their corresponding $\Delta G_{0.3125\rightarrow0.4375}$ at 400 °C as the target property. The performance of each learning algorithm with respect to the time-consumption, mean-absolute-error (MAE) and Pearson correlation coefficient (PCC) between the predicted and DFT computed values were presented in Fig. 5a. Results show that the time-consumption in the training step of all the considered algorithms are negligible, with the slowest one (gaussian process) takes only ~1 s to complete. The accuracies of the linear and polynomial regression algorithms are much lower than other algorithms, indicating that the underlying relationships between compositions and ΔGs, like many other quantum chemical problems, are non-linear and cannot be accurately described with linear or polynomial functions. The advantage of most no-linear algorithms is that they mainly contain multiple hyperparameters, i.e. internal model parameters, which can be optimized to adapt to different systems. This allows them to perform well in the current datasets. Especially the random forest (RF),[82] an ensemble learning algorithm based on a multitude of trainable decision trees, has shown superior prediction performances than many other non-linear algorithms like kernel-based ones in handling complex chemical and material problems.[83-86] As can be seen in Fig. 5a, RF exhibits the best predictive performance (highest PCC and lowest MAE) for the test datasets. It was therefore selected for subsequent training and predictions.

Fig. 5b summarizes the performance of RF on the test datasets in the model evaluation step. As can be seen, RF provides reasonable prediction accuracy for all the ΔGs considered with high PCC (0.813 – 0.952) and low MAE (0.284 – 0.657 eV). This is especially the case for $\Delta G_{0.3125\rightarrow0.4375}$ at both low (400 °C) and high (950 °C) temperatures, with high PCCs (0.952 and 0.943) and low MAEs (0.284 and 0.324 eV). Such errors, although higher than those for well-defined monometallic oxides, are comparable with typical DFT errors for mixed oxides containing 4 or more cations,[42] showing the RF model's potential. In addition, we also attempted to improve the RF model using additional μ_{O2}-related properties, such as the average charge (Δe) and p-band center (ε_p) of oxygen anions, as the input features in the model training step. However, Fig. S4 shows that the introduction of these electronic descriptors did not result in notable improvement of the predictive performances of the RF model. Considering the substantial CPU-time required for the calculations of these descriptors, we elected to not use them in the subsequent predictions.

ARTICLE

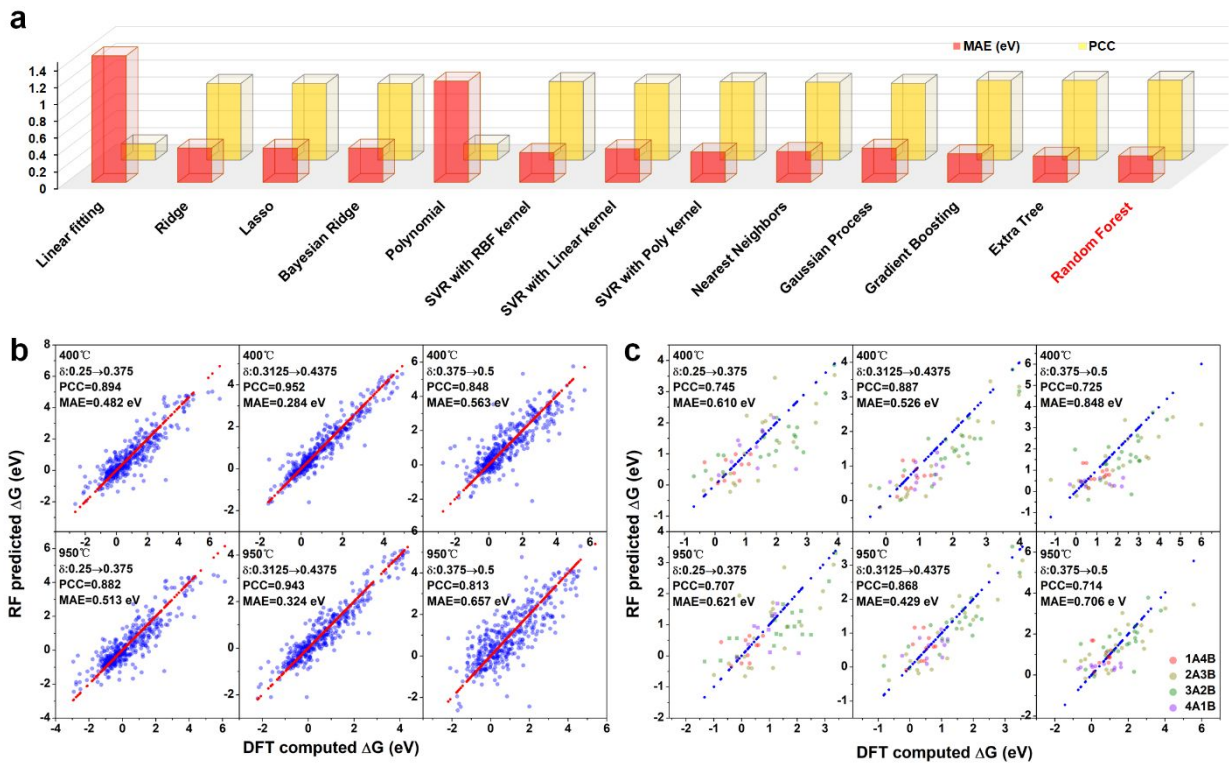

Fig. 5 Machine learning results. (a) PCC and MAE of different supervised ML algorithms. (b) Comparison of ΔG values computed by DFT with those predicted by RF within studied δ ranges at 400 and 950 °C. (c) DFT Verification of RF predicted ΔGs for 60 randomly selected datasets containing 5 cation elements. Here the RF model trained from the 2003 samples containing 2 – 4 cation elements were used to predict the ΔGs of the samples containing 5 cation elements.

Since the DFT calculation has already exhausted all the perovskites containing 2, 3, and 4 cation elements, we further extended the RF based ML model to predict the properties of perovskites containing 5 or more cation elements. These perovskites with five or more cations, also known as high-entropy perovskites (HEPs),[71] are an emerging class of new materials with unique redox properties and stability for various thermochemical applications.[87] Herein, 227,273 high-entropy perovskite compositions, prescreened out of 264,110 compositions based on the Goldschmidt's tolerance factor, were calculated. We elected not to use the modified tolerance factor for the preliminary screening due to the high complexity of the 5 cation elements perovskites, especially for those containing 4 B-site cations ($SrFe_{1-y1-y2-y3}B1_{y1}B2_{y2}B3_{y3}O_{3-\delta}$), which greatly increase the degree of uncertainties. In comparison, the applicability of the Goldschmidt's tolerance factor in high-entropy oxides with 5+ cations has been extensively examined.[88,89] To examine the reliability and accuracy of these predictions, we randomly selected 60 samples for further DFT calculations and compared the results with the predicted values as shown in Fig. 5c. The results confirm satisfactory correlations especially for the predictions of $\boldsymbol{\Delta G_{0.3125\rightarrow0.4375}}$ with PCC = 0.887 and 0.868, and MAE = 0.526 and 0.429 eV at 400 °C and 950 °C respectively. Such prediction accuracy is acceptable especially when applied to screen CL materials with large chemical potential spans such as CL CO_2 splitting. Combined with its efficiency (6 orders of magnitude faster than DFT calculations to produce a set of target ΔGs as shown in Fig. S5), ML can be a powerful tool for accelerated material discovery and design. However, further extension of the RF model to predict the property of more complex perovskites, such as the ones containing 6 or more cation elements, becomes unreliable (Fig. S6). This is probably because the chemical information contained in the current RF model is insufficient to predict the very complicated couplings of spin and electronic states in systems containing 6 or more cation elements. Although the current ML models are less than perfect due largely to the complexity of the mixed oxide system, it does provide an effective toolkit to greatly reduce experimental trial and error.

2.4 Applications for Chemical Looping Air Separation and CO2 splitting

The applicability and effectiveness of DFT and ML based high throughput screening are experimentally investigated in the context of chemical looping air separation (CLAS) and CL based CO_2 splitting. These two specific applications were selected since they represent two extreme chemical looping cases in terms of P_{O2} and operating temperature, as illustrated in Fig. 1b and Table 2 below. Covering the two extreme cases, with a 550 °C temperature span and 20 orders of magnitudes for P_{O2}, would help to demonstrate the general applicability of the computational results.

Table 2 Experimental parameters and screening criteria of CLAS and CL CO_2 splitting.

Application	*CLAS*	*CL CO_2 Splitting*
Reduction Rxn.	Air ⇆ N_2	$Sr_xA_{1-x}Fe_yB_{1-y}O_{3-\delta1}$ ⇆ $(\delta_2-\delta_1)/2\ O_2 + Sr_xA_{1-x}Fe_yB_{1-y}O_{3-\delta2}$
	$Sr_xA_{1-x}Fe_yB_{1-y}O_{3-\delta1}$ ⇆ $(\delta_2-\delta_1)/2\ O_2 + Sr_xA_{1-x}Fe_yB_{1-y}O_{3-\delta2}$	CO_2 ⇆ $CO + 1/2\ O_2$
Oxidation Rxn.	$(\delta_2-\delta_1)/2\ O_2 + Sr_xA_{1-x}Fe_yB_{1-y}O_{3-\delta2}$ ⇆ $Sr_xA_{1-x}Fe_yB_{1-y}O_{3-\delta1}$	$CH_4 + 1/2\ O_2$ ⇆ $CO + 2H_2$
		$(\delta_2-\delta_1)/2\ O_2 + Sr_xA_{1-x}Fe_yB_{1-y}O_{3-\delta2}$ ⇆ $Sr_xA_{1-x}Fe_yB_{1-y}O_{3-\delta1}$
P_{O2} range	~0.01 – 0.2 atm	~10^{-21} – 10^{-17} atm
Temp. range	400 – 900 ℃ (preferably <600 ℃)	750 – 1,000 ℃
Ideal ΔG ranges	0.05 – 0.13 eV at 400 ℃	2.23 – 2.24 eV at 400 ℃
	0.07 – 0.19 eV at 700 ℃	2.13 – 2.41 eV at 700 ℃
ΔG screening criteria	-0.25 – 0.63 eV at 400 ℃	1.93 – 2.74 eV at 400 ℃
	-0.23 – 0.69 eV at 700 ℃	1,83 – 2.91 eV at 700 ℃

CLAS operates within very narrow P_{O2} swings since the thermodynamic driving force for separating O_2 from air is intrinsically limited. The target range of ΔG per O atom can be calculated from the P_{O2} (or μ_{O2}) swing:[33,38]

$$\Delta G_{exp} = -\frac{1}{2}RT\ln\frac{P_{O_2}}{P^0}$$

where R is the ideal gas constant and P^0 is the standard atmospheric pressure. A P_{O2} swing between 0.01 and 0.2 atm is typical when considering both the oxygen release and regeneration requirements. This corresponds to very small ΔG ranges of 0.05 – 0.13 eV at 400 °C, and 0.07 – 0.19 eV at 700 °C. The narrow ranges are challenging for DFT due to its relatively large errors when calculating redox thermodynamics of perovskites (up to 0.98 eV) according to previous reports,[42] let alone the ML predictions which would have even larger errors. The errors from the DFT calculations in the current study are relatively small (0.05 ~ 0.70 eV) based on a comparison between the calculated results of 9 samples with those reported in experimental literatures (Table S3). The higher accuracy compared to previous DFT studies may have resulted from (1) the δ ranges investigated are closer to the experimental ranges; (2) the model created was based on an advanced sampling method (MCSQS), allowing the model to better represent a randomly distributed solid solution; (3) more accurate thermodynamic analyses were applied to estimate the enthalpy and entropy contributions.

Given that the goal of the high throughput calculation is to screen out promising materials, target ΔG ranges are relaxed to account for the uncertainty in DFT results. We note that DFT tends to overestimate the ΔG (Table S3), the upper limit of ΔG_{exp} were modified empirically by adding 0.5 eV while extending the lower limit by 0.3 eV. As such, the target ΔG ranges are modified to ΔG_{Target} $\begin{cases} \in [-0.25, 0.63]\ eV\ at\ 400℃ \\ \in [-0.23, 0.69]\ eV\ at\ 700℃ \end{cases}$. Using these target ranges, the promising materials were screened as shown in Fig. 6a and Fig. S7, in which the blue and red colors represent the samples whose ΔGs are higher or lower than the target region, respectively. Table S4 lists 1,270 candidates whose ΔGs are within the target range at either temperature. These materials have the potential for CLAS either at 400 or 700 °C. When applying a tighter criterion requiring satisfactory ΔGs at both 400 and 700 °C covering the entire δ range of 0.25 – 0.5, 113 promising CLAS candidates were further screened out, as listed in Table S5. Using the same target ΔG ranges, 17047 samples with 5 cation elements were predicted by ML as attached in our GitHub repositories.[90]

ARTICLE

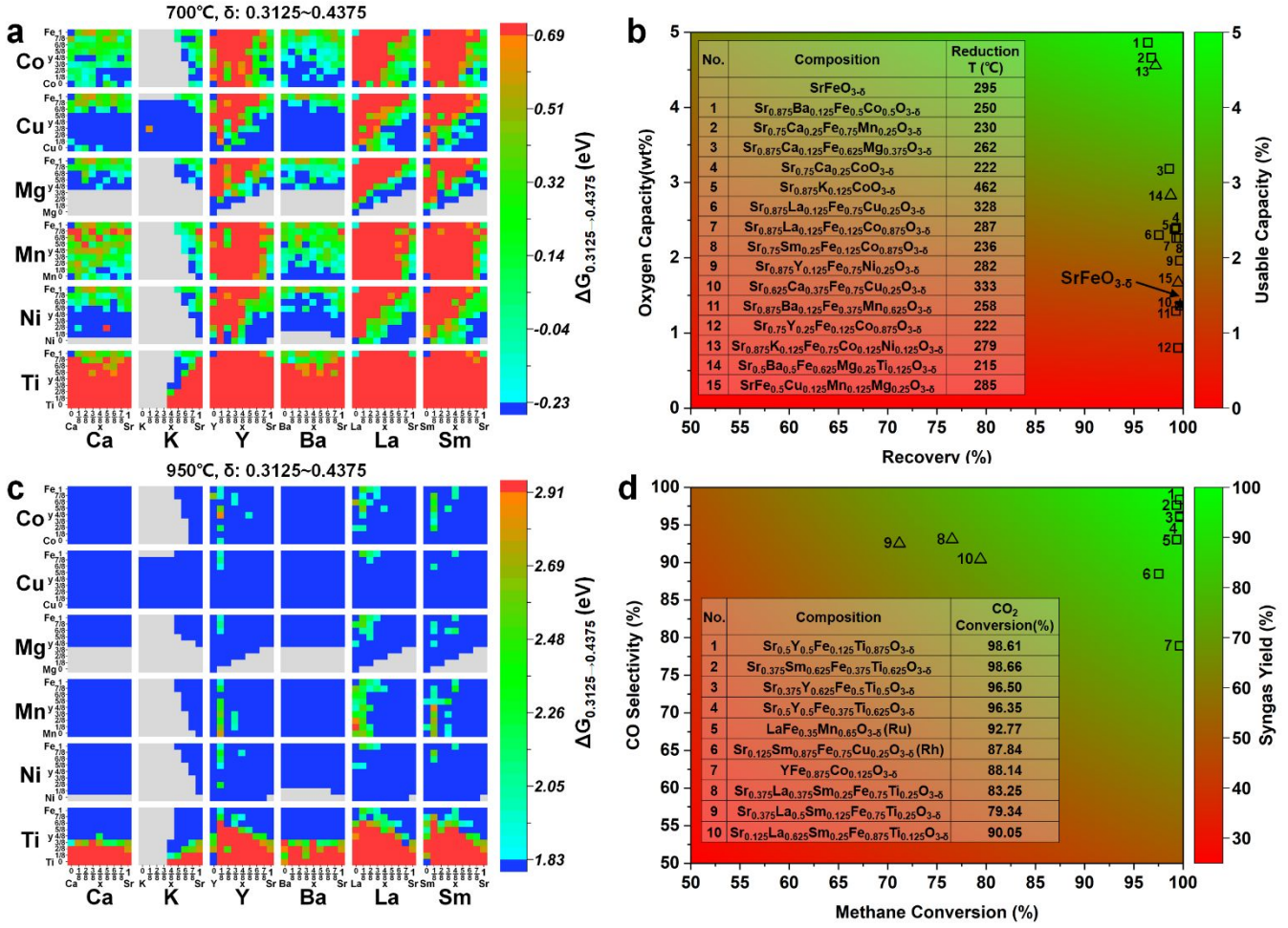

Fig. 6 High throughput screening results and experimental validations. (a) A heatmap of the screened candidates for CLAS at 700 °C within the δ range of 0.3125 ~ 0.4375 (heatmaps for the other temperature and δ ranges are shown in the supplemental document). (b) Experimental oxygen capacity, recovery, and usable capacity of the samples tested for CLAS. Squares and circles represent DFT and ML predicted samples, respectively. (c) A heatmap of the screened promising candidates for CL CO_2/H_2O splitting at 950 °C within the δ range of 0.3125 ~ 0.4375. (d) Experimental syngas yield and CO_2 conversion of the samples tested for CL CO_2 splitting. Squares and circles represent the DFT and ML predicted samples, respectively. In (a) and (c), the candidates whose ΔGs are within target ΔG regions ([-0.23,0.69] eV for CLAS and [-1.83,2.91] eV for CO_2 splitting) are plotted with the colors from cyan to orange as illustrated with the color bars. The species whose ΔGs above or below the target regions are plotted using red and blue, respectively. The grey areas refer to the 398 excluded unstable compositions.

Of the 113 CLAS materials predicted by DFT, 11 with very similar compositions have been confirmed by previous experimental systems and showed excellent results.[68,91-99] Of the 77 DFT predicted materials that have not been reported previously, we selected 12 materials for experimental validation. We also experimentally investigated 3 ML predicted materials. These experimental findings, both from literature and the current experimental study, are summarized in Table 3. Given that experimental procedures in literatures tend to vary, Fig. 6b only summarized the performance of the 15 samples tested in the present study using an identical testing procedure, where recovery is the percentage of the post cycle sample weight relative to the pre cycle weight, and usable capacity is defined as the recoverable oxygen capacity within each cycle. Table 3 summarized the performance details of the 11 literature reported materials as well as the 15 samples tested in this study.

As can be seen, a large fraction of the DFT predicted materials demonstrated satisfactory CLAS performance: 13 out of the 15 samples experimentally tested in this work exhibited better performance than the baseline $SrFeO_3$ oxygen carrier in at least one of the performance metrics; 10 samples are far superior (>50% increase in capacity *vs.* $SrFeO_3$). In addition, 5 of the 15 materials we tested demonstrated better performance than most, if not all, the previously reported materials. Interestingly, some of the compositions, such as $Sr_{0.875}Ca_{0.125}Fe_{0.625}Mg_{0.375}O_{3-\delta}$ and $Sr_{0.875}K_{0.125}Fe_{0.75}Co_{0.125}Ni_{0.125}O_{3-\delta}$, are quite atypical when compared to the compositions reported in literature. Investigation of these unique compositions would have been extremely unlikely if heuristic-based or trial and error approaches are adopted. This clearly demonstrates the effectiveness of the high throughput approach in this study. While it is not within the scope of this study to extensively test the ML predicted materials, our experimental results do indicate that ML can also provide valuable guidance on the design of complex mixed oxides. A few other high-entropy perovskite compositions predicted in this study were also examined as listed in Table S6, further confirming the effectiveness of the ML model. Experimental XRD patterns of the 15 samples are shown in Fig. S8, showing that their main phases are perovskites with some samples contain minor phase impurities. We also note that the poor-performance by $Sr_{0.875}Ba_{0.125}Fe_{0.375}Mn_{0.625}O_{3-\delta}$ is probably caused by phase segregation, with notable SrO and BaO phases (Fig. S8). This is likely to be due the hygroscopic nature of the Mn nitrate precursor, leading to lower amounts of Mn being incorporated into the perovskite. This issue occurred for all materials with Mn on the B site, including $SrFe_{0.5}Co_{0.125}Mn_{0.125}Mg_{0.25}O_{3-\delta}$ and $Sr_{0.75}Ca_{0.25}Fe_{0.75}Mn_{0.25}O_{3-\delta}$. The Ti containing phase suffered from a similar issue, as the Ti butoxide precursor, a viscous liquid, tends to aggregate along the walls of the transfer vessel. $Sr_{0.625}Ca_{0.375}Fe_{0.75}Cu_{0.25}O_{3-\delta}$ also suffers from phase segregation, with CuO and CaO both presenting in the XRD spectra. Segregation of CuO from perovskite was commonly encountered in previous literature.[92] It is also noted that many of these compositions, although appear to be complex, can be prepared by relatively simple methods such as solid-state reaction due to their thermodynamic stability. The capacity, recovery, and initial temperature of weight loss were also collected using a thermogravimetric analyzer (TGA) for six representative samples (Fig. S9), showing the process of oxygen release and uptake in a reaction cycle.

A similar screening method was adopted for CL CO_2-splitting. From a thermodynamic perspective, a high equilibrium P_{O2} leads to low CO_2 conversion in the splitting step and over oxidation of the syngas product in the methane POx step. In contrast, a low P_{O2} can lead to low methane conversion. An optimal range of P_{O2}, illustrated in Fig. 1b, can be calculated via Gibbs free energy minimization.[63] This corresponds to a target range of $\Delta \boldsymbol{G_{exp}} \begin{cases} \in [\mathbf{2.23}, \mathbf{2.24}]\ \boldsymbol{eV\ at}\ \mathbf{800}^{\circ}\mathrm{C} \\ \in [\mathbf{2.13}, \mathbf{2.41}]\ \boldsymbol{eV\ at}\ \mathbf{950}^{\circ}\mathrm{C} \end{cases}$ (Fig. S10). To account for DFT calculation errors, the target ΔG ranges are relaxed to $\Delta \boldsymbol{G_{target}} \begin{cases} \in [\mathbf{1.93}, \mathbf{2.74}]\ \boldsymbol{eV\ at}\ \mathbf{800}^{\circ}\mathrm{C} \\ \in [\mathbf{1.83}, \mathbf{2.91}]\ \boldsymbol{eV\ at}\ \mathbf{950}^{\circ}\mathrm{C} \end{cases}$. Promising candidates that fall within this target ΔG range are shown in Fig. 6c and Fig. S11. Table S7 lists 482 candidates with ΔGs within the target range at least under one of the temperatures. Under a tighter criterion of satisfactory ΔGs at both 800 and 950 °C for δ between 0.25 and 0.5, 30 promising candidates were identified (Table S8). For some samples with larger $\boldsymbol{\Delta G_{0.25\rightarrow 0.375}}$ (> 3 eV), their δs are not likely to reach above 0.25. Therefore, δ ranges of 0– 0.125, 0.125 – 0.25, and 0.0625 – 0.1875 were also taken into account as listed in Table S9, leading to 55 additional samples that are promising. Using the same criteria, 4267 samples with 5 cation elements were predicted by ML.[90]

Of the 85 materials predicted by DFT, 4 with very similar compositions have been reported in experimental literature and showed excellent results.[100-102] 4 additional previously reported compositions were covered by the loose criteria (Table S7).[103-107] The lack of literature reports compared to CLAS materials is largely due to relatively few studies on this subject. Of the 81 DFT predicted materials that have not been reported previously, we synthesized 7 for experimental validation. 3 ML predicted materials were also investigated experimentally. These experimental findings are summarized in Table 4. Fig. 6d illustrates the performances of the 10 samples tested in the present study. As can be seen, all 7 DFT-predicted samples exhibited >80% syngas yield and >85% CO_2 conversion, where Ru and Rh impregnations are used for two samples to promote the reaction rates without affecting the redox thermodynamics.[13,108,109] And all 3 ML-predicted samples exhibited >70% syngas yield and >80% CO_2 conversion. Nearly all these samples are in line with or superior to previously reported materials. It is noted that we successfully predicted and experimentally verified a family of perovskite materials with substantial amount of Ti doping in the B-site, such as $Sr_{0.5}Y_{0.5}Fe_{0.125}Ti_{0.875}O_{3-\delta}$ and $Sr_{0.375}Sm_{0.625}Fe_{0.375}Ti_{0.625}O_{3-\delta}$, and they showed outstanding CL CO_2-splitting performances. These materials would unlikely to be investigated without the high throughput study. The main phases of the 10 samples are all perovskites with some of them contains minor impurities, as verified by XRD (Fig. S12). The performance of the methane POx and CO_2 splitting steps are determined with mass spectrometry for three representative samples as shown in Fig. S13, again showing the excellent redox properties of our predicted oxygen carriers.

It is worth noting that there are groups of materials that require higher degree of reduction in the presence of CH_4, some of which can even reduce part of the perovskite parent structure to metals, like $La_{0.6}Sr_{0.4}Cr_{0.8}Co_{0.2}O_{3-\delta}$[110] and the composite material $LaNi_{0.35}Fe_{0.65}O_3$-$Ce_{0.85}Gd_{0.1}Cu_{0.05}O_{2-\delta}$.[111]. However, we note that while the search for active metal ex-solution criterion from a DFT standpoint is an interesting topic, it is beyond the scope of this study. The present study focuses

exclusively on the tunability of P_{O2}s for perovskite materials without phase transitions beyond brownmillerite.

ARTICLE

Table 3 Experimental performance of the DFT/ML predicted materials for CLAS

$Sr_{1-x}A_xFe_{1-y}B_yO_3$	Reference Data Source	Experimental Composition	DFT/ML Predicted Composition	Experimental Temperature	Experimental Environment	Key Experimental Results*
$SrFeO_3$	This study	Base Material	N/A	100 - 1000 °C	50% O_2	1.38 wt% R = 99.9% TR = 297 °C
A= Ca	Ref. 91	$Sr_{0.76}Ca_{0.24}FeO_{3-\delta}$	$Sr_{0.875}Ca_{0.125}FeO_{3-\delta}$ (DFT)	600 °C	5%-20% O_2	1.2 wt%
A= K	Ref. 93	$Sr_{0.9}K_{0.1}FeO_{3-\delta}$	$Sr_{0.875}K_{0.125}FeO_{3-\delta}$, $Sr_{0.625}K_{0.375}FeO_{3-\delta}$ (DFT)	700 °C	1%-20% O_2	1.35 wt%
B= Cu	Ref. 92,97	$SrFe_{0.85}Cu_{0.15}O_{3-\delta}$	$SrFe_{0.75}Cu_{0.25}O_{3-\delta}$ (DFT)	350 - 1000 °C	90%-0.01% O_2	~2.9 wt%
B= Mn	Ref. 93,94	$SrFe_{0.9}Mn_{0.1}O_{3-\delta}$	$SrFe_{0.625}Mn_{0.375}O_{3-\delta}$ (DFT)	700 °C	1%-20% O_2	1.33 wt%
A=Ba; B=Co	Ref. 96	$Sr_{0.9}Ba_{0.1}Fe_{0.8}Co_{0.2}O_{3-\delta}$, $Sr_{0.7}Ba_{0.3}Fe_{0.8}Co_{0.2}O_{3-\delta}$, $Sr_{0.5}Ba_{0.5}Fe_{0.8}Co_{0.2}O_{3-\delta}$	$Sr_{0.75}Ba_{0.25}Fe_{0.75}Co_{0.25}O_{3-\delta}$ (DFT) $Sr_{0.75}Ba_{0.25}Fe_{0.5}Co_{0.5}O_{3-\delta}$ (DFT) $Sr_{0.5}Ba_{0.5}Fe_{0.5}Co_{0.5}O_{3-\delta}$ (DFT)	500 - 1300 K	N_2	~1.7 wt%
A=Ca; B=Co	Ref. 53,70	$Sr_{0.8}Ca_{0.2}Fe_{0.4}Co_{0.6}O_{3-\delta}$	$Sr_{0.75}Ca_{0.25}Fe_{0.375}Co_{0625}O_{3-\delta}$ (DFT)	400 °C	5%-20% O_2	1.2 wt%
A=Ca; B=Mn	Ref. 97	$Sr_{0.2}Ca_{0.8}MnO_{3-\delta}$	$Sr_{0.625}Ca_{0.375}Fe_{0.25}Mn_{0.75}O_{3-\delta}$ (DFT)	1200 - 400 °C	Ar	2.25 wt%
A=La; B=Co	Ref. 68,98,99	$Sr_{0.9}La_{0.1}Fe_{0.1}Co_{0.9}O_{3-\delta}$, $Sr_{0.9}La_{0.1}Fe_{0.5}Co_{0.5}O_{3-\delta}$	$Sr_{0.875}La_{0.125}Fe_{0.125}Co_{0.875}O_{3-\delta}$ (DFT) $Sr_{0.875}La_{0.125}Fe_{0.5}Co_{0.5}O_{3-\delta}$ (DFT)	25 - 800 °C	He	2.5 wt%

A=Ba; B=Co	This Study	$Sr_{0.875}Ba_{0.125}Fe_{0.5}Co_{0.5}O_{3-\delta}$	$Sr_{0.875}Ba_{0.125}Fe_{0.5}Co_{0.5}O_{3-\delta}$ (DFT)	100 - 1000 °C	50% O_2	4.86 wt% R = 96.7% TR = 250 °C
A=Ca; B=Mn	This Study	$Sr_{0.75}Ca_{0.25}Fe_{0.75}Mn_{0.25}O_{3-\delta}$	$Sr_{0.75}Ca_{0.25}Fe_{0.75}Mn_{0.25}O_{3-\delta}$ (DFT)	100 - 1000 °C	50% O_2	4.66 wt% R = 97% TR = 230 °C
A=Ca; B=Mg	This Study	$Sr_{0.875}Ca_{0.125}Fe_{0.625}Mg_{0.375}O_{3-\delta}$	$Sr_{0.875}Ca_{0.125}Fe_{0.625}Mg_{0.375}O_{3-\delta}$ (DFT)	100 - 1000 °C	50% O_2	3.18 wt% R = 98.9% TR = 262 °C
A=Ca; B=Co	This Study	$Sr_{0.75}Ca_{0.25}CoO_{3-\delta}$	$Sr_{0.75}Ca_{0.25}CoO_{3-\delta}$ (DFT)	100 - 1000 °C	50% O_2	2.4 wt% R = 99.6% TR = 222 °C
A=K; B=Co	This Study	$Sr_{0.875}K_{0.125}CoO_{3-\delta}$	$Sr_{0.875}K_{0.125}CoO_{3-\delta}$ (DFT)	100 - 1000 °C	50% O_2	2.38 wt% R = 99% TR = 262 °C
A=La; B=Cu	This Study	$Sr_{0.875}La_{0.125}Fe_{0.75}Cu_{0.25}O_{3-\delta}$	$Sr_{0.875}La_{0.125}Fe_{0.75}Cu_{0.25}O_{3-\delta}$ (DFT)	100 - 1000 °C	50% O_2	2.3 wt% R = 97.8% TR = 328 °C
A=La; B=Co	This Study	$Sr_{0.875}La_{0.125}Fe_{0.125}Co_{0.875}O_{3-\delta}$	$Sr_{0.875}La_{0.125}Fe_{0.125}Co_{0.875}O_{3-\delta}$ (DFT)	100 - 1000°C	50% O_2	2.26 wt% R = 99.9% TR = 287 °C
A=Sm; B=Co	This Study	$Sr_{0.75}Sm_{0.25}Fe_{0.125}Co_{0.875}O_{3-\delta}$	$Sr_{0.75}Sm_{0.25}Fe_{0.125}Co_{0.875}O_{3-\delta}$ (DFT)	100 - 1000 °C	50% O_2	2.26 wt% R = 99.6% TR = 236 °C
A=Y; B=Ni	This Study	$Sr_{0.875}Y_{0.125}Fe_{0.75}Ni_{0.25}O_{3-\delta}$	$Sr_{0.875}Y_{0.125}Fe_{0.75}Ni_{0.25}O_{3-\delta}$ (DFT)	100 - 1000 °C	50% O_2	1.96 wt% R = 100% TR = 282 °C
A=Ca; B=Cu	This Study	$Sr_{0.625}Ca_{0.375}Fe_{0.75}Cu_{0.25}O_{3-\delta}$	$Sr_{0.625}Ca_{0.375}Fe_{0.75}Cu_{0.25}O_{3-\delta}$ (DFT)	100 - 1000 °C	50% O_2	1.36 wt% R = 100% TR = 333 °C
A=Ba; B=Mn	This Study	$Sr_{0.875}Ba_{0.125}Fe_{0.375}Mn_{0.625}O_{3-\delta}$	$Sr_{0.875}Ba_{0.125}Fe_{0.375}Mn_{0.625}O_{3-\delta}$ (DFT)	100 - 1000 °C	50% O_2	1.29 wt% R = 99.6 TR = 258 °C

A=Y; B=Co	This Study	$Sr_{0.75}Y_{0.25}Fe_{0.125}Co_{0.875}O_{3-\delta}$	$Sr_{0.75}Y_{0.25}Fe_{0.125}Co_{0.875}O_{3-\delta}$ (DFT)	100 - 1000 °C	50% O_2	0.80 wt% R = 99.8% TR = 222 °C
A=K; B_1=Co, B_2=Ni	This Study	$Sr_{0.875}K_{0.125}Fe_{0.75}Co_{0.125}Ni_{0.125}O_{3-\delta}$	$Sr_{0.875}K_{0.125}Fe_{0.75}Co_{0.125}Ni_{0.125}O_{3-\delta}$ (ML)	100 - 1000 °C	50% O_2	4.56 wt% R = 97.5% TR = 279 °C
A=Ba; B_1=Mg, B_2=Ti	This Study	$Sr_{0.5}Ba_{0.5}Fe_{0.625}Mg_{0.25}Ti_{0.125}O_{3-\delta}$	$Sr_{0.5}Ba_{0.5}Fe_{0.625}Mg_{0.25}Ti_{0.125}O_{3-\delta}$ (ML)	100 - 1000 °C	50% O_2	2.83 wt% R = 99% TR = 215 °C
B_1=Cu, B_2=Mn, B_3=Mg	This Study	$SrFe_{0.5}Cu_{0.125}Mn_{0.125}Mg_{0.25}O_{3-\delta}$	$SrFe_{0.5}Cu_{0.125}Mn_{0.125}Mg_{0.25}O_{3-\delta}$ (ML)	100 - 1000 °C	50% O_2	1.67 wt% R = 99.8% TR = 285 °C

* The first number refers to weight-based oxygen capacity, R refers to percent of recoverable oxygen capacity, TR refers to the initial reduction temperature.

Table 4 Experimental performance of the DFT/ML predicted materials for CL CO_2-splitting.

$Sr_{1-x}A_xFe_{1-y}B_yO_3$	Reference Data Source	Experimental Composition	DFT/ML Predicted Composition	Temperature	Gas Flow (mL/min)	Results*
A= La	Ref. 103, 100	$LaFeO_{3-\delta}$, $Sr_{0.3}La_{0.7}FeO_{3-\delta}$	$LaFeO_{3-\delta}$[a] (DFT) $Sr_{0.25}La_{0.75}FeO_{3-\delta}$ (DFT)	850 °C	CH_4/N_2=20/30 H_2O/N_2=578/50	X_{CH4} ~ 50-80% S_{CO} ~ 90%
A=La; B=Co	Ref. 101	$LaFe_{0.7}Co_{0.3}O_{3-\delta}$, $LaFe_{0.5}Co_{0.5}O_{3-\delta}$, $LaFe_{0.3}Co_{0.7}O_{3-\delta}$	$Sr_{0.125}La_{0.875}Fe_{0.5}Co_{0.5}O_{3-\delta}$ (DFT)	850 °C	CH_4/N_2=20/30 H_2O/N_2=578/50	X_{CH4} ~ 90% S_{CO} ~ 45%
A=La; B=Mn	Ref. 102	$LaFe_{0.7}Mn_{0.3}O_{3-\delta}$, $LaFe_{0.5}Mn_{0.5}O_{3-\delta}$	$LaFe_{0.375}Mn_{0.625}O_{3-\delta}$ $LaFe_{0.625}Mn_{0.375}O_{3-\delta}$ (DFT)	850 °C	CH_4/N_2=20/30 H_2O/N_2=578/50	X_{CH4} ~ 90% S_{CO} ~ 95% H_2 generation capacity ~ 4 mmol/g
A=La; B=Ni	Ref. 104	$LaFe_{0.9}Ni_{0.1}O_{3-\delta}$	$LaFe_{0.75}Ni_{0.25}O_{3-\delta}$[a] (DFT)	850 °C	CH_4/N_2=20/30 H_2O/N_2=578/50	X_{CH4} ~ 90%
A=La; B=Ni	Ref. 105	$LaFe_{0.65}Ni_{0.35}O_{3-\delta}$	$LaFe_{0.625}Ni_{0.375}O_{3-\delta}$[a] (DFT)	750 °C	CH_4/N_2=2.8/25 CO_2/N_2=1/25	X_{CH4} = 31% S_{CO} = 90% X_{CO2} = 37%
A=La; B=Ni	Ref. 106	$LaFe_{0.5}Ni_{0.5}O_{3-\delta}$	$LaFe_{0.5}Ni_{0.5}O_{3-\delta}$[a] (DFT)	700 °C	CH_4/N_2=2.8/25 CO_2/Ar=1.4/25	X_{CH4} ~ 90% S_{CO} > 90% X_{CO2} ~ 90%

A=La; B1=Cr; B2=Co	Ref. 29	$La_{0.6}Sr_{0.4}Cr_{0.8}Co_{0.2}O_{3-\delta}$	Cr is not considered in this study	900 °C	CH_4/N_2=0.75/14.25 CO_2/N_2=48/252	CO production rate ~ 100 mL min^{-1} g^{-1}
A=La; B=Cr	Ref. 107	$Sr_{0.3}La_{0.7}Fe_{0.9}Cr_{0.1}O_{3-\delta}$	Cr is not considered in this study	1000 °C	CH_4/H_2O Pulse experiment	X_{CH4} ~ 70%
A=Y; B=Ti	This Study	$Sr_{0.5}Y_{0.5}Fe_{0.125}Ti_{0.875}O_{3-\delta}$	$Sr_{0.5}Y_{0.5}Fe_{0.125}Ti_{0.875}O_{3-\delta}$ (DFT)	950 °C	CH_4/N_2=2.5/22.5 CO_2/N_2=2.5/22.5	X_{CH4} ~ 100% S_{CO} = 98% X_{CO2} = 99% Y_{syngas} = 98% Oxygen capacity = 0.70 wt%
A=Y; B=Ti	This Study	$Sr_{0.375}Y_{0.625}Fe_{0.5}Ti_{0.5}O_{3-\delta}$	$Sr_{0.375}Y_{0.625}Fe_{0.5}Ti_{0.5}O_{3-\delta}$ (DFT)	950 °C	CH_4/N_2=2.5/22.5 CO_2/N_2=2.5/22.5	X_{CH4} ~ 100% S_{CO} = 96% X_{CO2} = 96% Y_{syngas} = 96% Oxygen capacity = 0.69 wt%
A=Y; B=Ti	This Study	$Sr_{0.5}Y_{0.5}Fe_{0.375}Ti_{0.625}O_{3-\delta}$	$Sr_{0.5}Y_{0.5}Fe_{0.375}Ti_{0.625}O_{3-\delta}$ (DFT)	950 °C	CH_4/N_2=2.5/22.5 CO_2/N_2=2.5/22.5	X_{CH4} ~ 100% S_{CO} = 96% X_{CO2} = 96% Y_{syngas} = 96% Oxygen capacity = 0.69 wt%
A=Sm; B=Ti	This Study	$Sr_{0.375}Sm_{0.625}Fe_{0.375}Ti_{0.625}O_{3-\delta}$	$Sr_{0.375}Sm_{0.625}Fe_{0.375}Ti_{0.625}O_{3-\delta}$ (DFT)	950 °C	CH_4/N_2=2.5/22.5 CO_2/N_2=2.5/22.5	X_{CH4} ~ 100% S_{CO} = 98% X_{CO2} = 99% Y_{syngas} = 97% Oxygen capacity = 0.70 wt%
A=La; B=Mn	This Study	$LaFe_{0.35}Mn_{0.65}O_{3-\delta}$ (1 wt% Ru impregnated)	$LaFe_{0.35}Mn_{0.65}O_{3-\delta}$ (DFT)	950 °C	CH_4/N_2=2.5/22.5 CO_2/N_2=2.5/22.5	X_{CH4} ~ 100% S_{CO} = 93% X_{CO2} = 93% Y_{syngas} = 93% Oxygen capacity = 0.66 wt%

A=Y; B=Co	This Study	$YFe_{0.875}Co_{0.125}O_{3-\delta}$	$YFe_{0.875}Co_{0.125}O_{3-\delta}$ (DFT)	950 °C	CH_4/N_2=2.5/22.5 CO_2/N_2=2.5/22.5	X_{CH4} ~ 100% S_{CO} = 80% X_{CO2} = 88% Y_{syngas} = 80% Oxygen capacity = 0.63 wt%
A=Sm; B=Cu	This Study	$Sr_{0.125}Sm_{0.875}Fe_{0.75}Cu_{0.25}O_{3-\delta}$ (0.5 wt% Rh impregnated)	$Sr_{0.125}Sm_{0.875}Fe_{0.75}Cu_{0.25}O_{3-\delta}$ (DFT)	950 °C	CH_4/N_2=2.5/22.5 CO_2/N_2=2.5/22.5	X_{CH4} = 98% S_{CO} = 89% X_{CO2} = 88% Y_{syngas} = 87% Oxygen capacity = 0.63 wt%
A_1=La, A_2=Sm; B=Ti	This Study	$Sr_{0.375}La_{0.375}Sm_{0.25}Fe_{0.75}Ti_{0.25}O_{3-\delta}$	$Sr_{0.375}La_{0.375}Sm_{0.25}Fe_{0.75}Ti_{0.25}O_{3-\delta}$ (ML)	950 °C	CH_4/N_2=2.5/22.5 CO_2/N_2=2.5/22.5	X_{CH4} = 77% S_{CO} = 93% X_{CO2} = 83% Y_{syngas} = 71% Oxygen capacity = 0.59 wt%
A_1=La, A_2=Sm; B=Ti	This Study	$Sr_{0.375}La_{0.5}Sm_{0.125}Fe_{0.75}Ti_{0.25}O_{3-\delta}$	$Sr_{0.375}La_{0.5}Sm_{0.125}Fe_{0.75}Ti_{0.25}O_{3-\delta}$ (ML)	950 °C	CH_4/N_2=2.5/22.5 CO_2/N_2=2.5/22.5	X_{CH4} = 71% S_{CO} = 93% X_{CO2} = 80% Y_{syngas} = 71% Oxygen capacity = 0.57 wt%
A_1=La, A_2=Sm; B=Ti	This Study	$Sr_{0.125}La_{0.625}Sm_{0.25}Fe_{0.875}Ti_{0.125}O_{3-\delta}$	$Sr_{0.125}La_{0.625}Sm_{0.25}Fe_{0.875}Ti_{0.125}O_{3-\delta}$ (ML)	950 °C	CH_4/N_2=2.5/22.5 CO_2/N_2=2.5/22.5	X_{CH4} = 80% S_{CO} = 90% X_{CO2} = 90% Y_{syngas} = 72% Oxygen capacity = 0.64 wt%

[a] denotes that these materials are screened with a loose criteria (Table S7).

* X_{CH4}, S_{CO}, X_{CO2}, Y_{syngas} represent methane conversion, CO selectivity, CO_2 conversion, and Syngas yield, respectively.

ARTICLE

Conclusions

Using $Sr_xA_{1-x}Fe_yB_{1-y}O_{3-\delta}$ as a model system, the present study developed and experimentally validated DFT and ML based high-throughput simulation approaches to rationally tailor the redox oxygen chemical potential of perovskite oxides. The DFT-based high-throughput model is shown to be effective to identify cation dopant types and concentrations to flexibly adjust the equilibrium oxygen partial pressures of the mixed oxides over 20 orders of magnitude (10^{-21} atm – 0.1 atm) and across a large temperature range (400 – 900 °C). Overall, the oxygen chemical potentials for 2401 perovskite oxides containing up to 4 cation elements were simulated as a function of their oxygen vacancy concentrations (δ). Using these results, 113 materials were predicted to be suitable for chemical looping air separation (CLAS) whereas 85 materials were projected to be ideal for CL based CO_2-splitting. The validity of these predictions from DFT was verified experimentally, both in the current study and through previous experimental literature. In total, 43 of the compositions predicted were verified in previous publications, showing excellent performance. Additionally, we prepared and evaluated 25 additional model predicted materials. Out of these, 23 oxygen carriers exhibited satisfactory performances, and 15 showed superior performance compared to most, if not all, the previously reported oxygen carriers. The DFT based high-throughput simulation results were further applied to develop a machine learning (ML) model, which showed satisfactory accuracy. Using the ML model, redox thermodynamics of 227,273 perovskites containing 5 cation elements were investigated, leading to ~20,000 promising oxygen carrier candidates. The prediction by the ML model was further validated by DFT calculations as well as experimental investigations of selected perovskite compositions. Interestingly, the DFT and ML based high-throughput approaches have led to many nonobvious oxygen carrier compositions with superior chemical looping performance, e.g. tripling the oxygen capacity *vs*. the benchmark oxygen carrier for CLAS. Discovery of these unique compositions, such as $Sr_{0.875}K_{0.125}Fe_{0.75}Co_{0.125}Ni_{0.125}O_{3-\delta}$ and $Sr_{0.375}La_{0.5}Sm_{0.125}Fe_{0.75}Ti_{0.25}O_{3-\delta}$, would be highly unlikely if one adopts conventional oxygen carrier design approaches. As such, the findings in the current study open up a new and effective strategy for rational design of high-performance oxygen carriers. It can also be generalized for tailoring the redox properties of complex oxides beyond chemical looping applications.

3. Computational and Experimental Methods

4.1 DFT Calculations

First-principles simulations were performed at the DFT level implemented by the Vienna *ab initio* Simulation package (VASP)[112] with the frozen-core all-electron projector augmented wave (PAW) model[113] and Perdew-Burke-Ernzerhof (PBE) functions.[114] A kinetic energy cutoff of 450 eV was used for the plane-wave expansion of the electronic wave function, and the convergence criterions of force and energy were set as 0.01 eV $Å^{-1}$ and 10^{-5} eV respectively. A Gaussian smearing of 0.1 eV was applied for optimizations. Gamma k-point was used for the 2 × 2 × 2 $Sr_xA_{1-x}Fe_yB_{1-y}O_{3-\delta}$ perovskite supercells, which contain 40-8δ atoms, to reduce the computational intensity. 1 × 2 × 2 Gamma-centered k-points were chosen for brownmillerite structures. The strong on-site coulomb interaction on the d-orbital electrons on the Fe, Co, Cu, Mn, Ni and Ti-sites were treated with the GGA+U approach[115] with U_{eff} = 4, 3.4, 4, 3.9, 6 and 3 respectively, which gave reasonable predictions of geometric and electronic structures based on previous reports.[116,117] To make the simulations tractable, only FM phase magnetic ordering was applied for all the doped structures given that magnetic ordering has relatively small effects on the oxygen vacancy formation and migration.[118] The initial spin moment for Fe, Co, Mn, Ni were set to 4, 5, 5, 5, respectively.

To make the $Sr_xA_{1-x}Fe_yB_{1-y}O_{3-\delta}$ models closer to randomly disordered solid solution phases, the Monte Carlo special quasirandom structures (MCSQS) method[119] was applied to determine the position of all A- and B-site dopants and oxygen vacancies. The vibrational related properties such as the zero-point energy (ZPE) and entropic contributions from phonons (S_{vib}) were computed within the harmonic approximation using the *Phonopy* code[120]. For an optimized $Sr_xA_{1-x}Fe_yB_{1-y}O_{3-\delta}$ crystal structure, a mixture of finite displacements and analytical gradients is used to construct a dynamical matrix of force constants, where forces were obtained from DFT calculations on a 2 × 2 × 2 supercell. The change in configurational entropy (S_{conf}) were estimated by $\Delta S_{conf} = aR[2\delta ln(2\delta) + (1-2\delta)\ln(1-2\delta)]$,[121] where *R* is the ideal gas constant and *a* is the factor referring to the interaction of oxygen vacancies with a = 2 describing an ideal solid solution with no defect interaction. For the solid-state perovskite and brownmillerite systems, since the contribution of *PV* term is negligible, the ΔG was approximated by $\Delta G = \Delta U - T(\Delta S_{vib} + \Delta S_{conf})$.[122,123]

To address the well-known overbinding issue of the O_2 molecule within DFT, enthalpy of O_2 is computed using $H_{O_2}(T) = 2H_O^{PAW/PBE}(T) + H_{binding}^{CBS-QB3}(T)$, in which $H_{binding}^{CBS-QB3}(T) = H_{O_2}^{CBS-QB3}(T) - 2H_O^{CBS-QB3}(T)$, where the CBS-QB3 method is implemented using Gaussian 16[124] (see Fig. S1 and Table S1 in Supplemental Information).

4.2 The ML protocol

All ML algorithms were implemented by Scikit-learn.[72] The random forest (RF) algorithm[82] was applied to establish the relationship between the selected features (the proportion of

each A and B site element) and target (ΔG within selected δ ranges) due to its robustness, noise tolerance, and ability to handle complex nonlinear relationships. The RF model is composed of 100 decision trees. Continue increasing the number of trees did not give improved prediction performances. The nodes are expanded until all leaves are pure or until all leaves contain less than 2 samples. A total number of 10,015 datasets were randomly divided into two parts: randomly selected 8,012 datasets were used for training and the remaining 2003 were used for testing. Since the data of features (element ratio) are already from 0 to 1, normalization was unnecessary. The accuracy and robustness of the final machine learning results were verified by a cross-validation technique[125]: all the datasets were randomly and evenly distributed into 5 bins in this procedure with each bin used as a test set while the remaining 4 bins as training sets. Prediction accuracy and errors were evaluated by Pearson correlation coefficients (*r*) and mean-absolute-errors (MAE).

4.3 Sample synthesis and characterization

All the materials were synthesized using a modified Pechini method. In a typical synthesis of $A_xA'_{1-x}B_xB'_{1-x}O_3$, stoichiometric amounts of the associated metal nitrates were dissolved in deionized water, roughly 15 mL. Then, citric acid was added to the solution at a molar ratio of 2.5 to 1 and stirred at room temperature for 30 min. In synthesis of Ti-containing materials in the B-site, stoichiometric amount of titanium (IV) butoxide was added into the solution. Then, ethanol was also added into the solution with a mass ratio of ethanol/titanium (IV) butoxide = 10/1. Next, ethylene glycol was added at a molar ratio of 1.5 (ethylene glycol) to 1 (citric acid), and the solution was heated to 80 °C and held for 3 h while being stirred until a gel is formed. The resulting material was heated in an oven at 120 °C for 16 h. The dried sample was calcined in air at 1,000 °C for 8 h to remove the organic compounds and to form the perovskite phase. Finally, the resulting sample was sieved to desired particle size ranges (150 - 250 μm for TGA testing and 250 – 450 μm for packed bed experiments). We note that Y doped samples needed a slightly lower sintering temperature (900°C for 10 hours). The crystalline phases of the materials synthesized were determined with powder X-ray diffraction (XRD) using a Rigaku SmartLab X-ray diffractometer with Cu Kα (λ=0.15418 nm). The radiation was operated at 40 kV and 44 mA. 2θ angle between 15-60 or 15-80° were used to scan for XRD patterns. All 25 samples prepared contain perovskite as the majority phase. Phase impurities were completely absent in 11 of them, negligibly small in 7, and notable in the remaining 7 samples (see Fig. S8 and S12).

4.4 Sample evaluation

CL Air Separation

The capacity, recovery, and initial temperature of weight loss were collected using a thermogravimetric analyzer (TGA Q650). Approximately 50 mg of material was added to an alumina sample cup and placed in the TGA. The flowrate was set to 200 sccm, 100 sccm of oxygen and 100 sccm of Ar, the balance gas. The oxygen concentration was also monitored using a Setnag oxygen analyzer. Initially, the material was heated to 600 °C slowly to remove any water or carbonates present in the material. Then, the program was devised to ramp at 20 °C/min to 1000 °C under a 50% oxygen environment, hold at 1,000 °C for 10 minutes, and then cool back to 100 °C at a same ramp rate.

CL CO_2 splitting

The reactivity performances of the synthesized materials were tested in a 1/8 in. ID packed-bed quartz U-tube reactor inside of a tubular furnace. Prior to testing, the materials were pelletized and sieved to 250-450μm diameter particle size. Then, 0.5 g of the sieved particles were placed into the U-tube. The furnace was then raised to 950°C under 25 mL/min of Ar flow. Then, an additional 2.8 mL/min CH_4 flow was added for 2 min as the CH_4 partial oxidation step. Then, the CH_4 flow was stopped, and the U-tube was purged with Ar for 5 mins. Subsequently, 1.4 mL/min of CO_2 was introduced for 4 mins as the CO_2 splitting step. After the CO_2 splitting step, the U-tube was purged with Ar again for 5 mins prior to the next cycle. The products were measured with a downstream quadruple mass spectroscopy (QMS, MKS Cirrus II). At least 10 cycles were conducted to assure that the reactive performances reach a steady state.

Author Contributions

Conceptualization, X.W. and F.L.; Methodology, X.W., Y.G., E.K., S.I., and F.L.; Investigation, X.W., Y.G., E.K., S.I., J.D., R.C., H.W., C.R., S.Y., and F.L.; Writing – Original Draft, X.W., Y.G., E.K., and F.L.; Writing – Review & Editing, X.W., Y.G., E.K., and F.L.; Funding Acquisition, F.L.; Resources, F.L.; Supervision, F.L.

Conflicts of interest

There are no conflicts to declare.

Acknowledgements

This work was supported by the U.S. Department of Energy (Award No. FE0031521), the National Science Foundation (Grant No. CBET-1510900), and the North Carolina State University Kenan Institute for Engineering, Technology, and Science. We acknowledge the use of the Analytical Instrumentation Facility (AIF) at North Carolina State University, which is supported by the State of North Carolina and the National Science Foundation.

References

1 K. Wang, Q. Yu, M. van Sint Annaland, T. Wu and Q. Qin, *Energy & Fuels*, 2020, **34**, 3449-3457.
2 C. Y. Lau, M. T. Dunstan, W. Hu, C. P. Grey and S. A. Scott, *Energy Environ. Sci.*, 2017, **10**, 818-831.
3 S. Bhavsar, M. Najera, R. Solunke and G. Veser, *Catal. Today*, 2014, **228**, 96-105.
4 D. Li, R. Xu, Z. Gu, X. Zhu, S. Qing and K. Li, *Energy Technology*, 2020, **8**, 1900925.
5 L.-S. Fan, L. Zeng, W. Wang and S. Luo, *Energy Environ. Sci.*, 2012, **5**, 7254-7280.
6 B. J. Hare, D. Maiti, Y. A. Daza, V. R. Bhethanabotla and J. N. Kuhn, *ACS Catalysis*, 2018, **8**, 3021-3029.

7 M. Bui, C. S. Adjiman, A. Bardow, E. J. Anthony, A. Boston, S. Brown, P. S. Fennell, S. Fuss, A. Galindo and L. A. Hackett, *Energy Environ. Sci.*, 2018, **11**, 1062-1176.
8 I. Al-Shankiti, B. D. Ehrhart and A. W. Weimer, *Solar Energy*, 2017, **156**, 21-29.
9 Y. A. Daza, R. A. Kent, M. M. Yung and J. N. Kuhn, *Industrial & Engineering Chemistry Research*, 2014, **53**, 5828-5837.
10 S. Chuayboon, S. Abanades and S. Rodat, *Frontiers in Energy Research*, 2020, **8**, 128.
11 L. Zeng, Z. Cheng, J. A. Fan, L.-S. Fan and J. Gong, *Nature Reviews Chemistry*, 2018, **2**, 349-364.
12 S. Chen, L. Zeng, R. Mu, C. Xiong, Z.-J. Zhao, C. Zhao, C. Pei, L. Peng, J. Luo and L.-S. Fan, *J. Am. Chem. Soc.*, 2019, **141**, 18653-18657.
13 X. Zhu, Q. Imtiaz, F. Donat, C. R. Müller and F. Li, *Energy Environ. Sci.*, 2020, **13**, 772-804.
14 L. Qin, M. Guo, Y. Liu, Z. Cheng, J. A. Fan and L.-S. Fan, *Applied Catalysis B: Environmental*, 2018, **235**, 143-149.
15 A. Shafiefarhood, N. Galinsky, Y. Huang, Y. Chen and F. Li, *ChemCatChem*, 2014, **6**, 790-799.
16 L. M. Neal, A. Shafiefarhood and F. Li, *ACS Catalysis*, 2014, **4**, 3560-3569.
17 A. Mishra, T. Li, F. Li and E. E. Santiso, *Chem. Mater.*, 2018, **31**, 689-698.
18 I. Adánez-Rubio, P. Gayán, A. Abad, F. García-Labiano, L. De Diego and J. Adánez, *Chem. Eng. J.*, 2014, **256**, 69-84.
19 B. Bulfin, J. Lapp, S. Richter, D. Guban, J. Vieten, S. Brendelberger, M. Roeb and C. Sattler, *Chem. Eng. Sci.*, 2019, **203**, 68-75.
20 S. Ma, S. Chen, A. Soomro and W. Xiang, *Energy & Fuels*, 2017, **31**, 8001-8013.
21 G. Deng, K. Li, G. Zhang, Z. Gu, X. Zhu, Y. Wei and H. Wang, *Applied Energy*, 2019, **253**, 113534.
22 Y. Long, Z. Gu, S. Lin, K. Yang, X. Zhu, Y. Wei, H. Wang and K. Li, *Journal of the Energy Institute*, 2021, **94**, 199-209.
23 V. P. Haribal, X. Wang, R. Dudek, C. Paulus, B. Turk, R. Gupta and F. Li, *Advanced Energy Materials*, 2019, **9**, 1901963.
24 N. Galinsky, M. Sendi, L. Bowers and F. Li, *Applied Energy*, 2016, **174**, 80-87.
25 Z. Miao, Z. Hu, E. Jiang and X. Ma, *Fuel*, 2020, **279**, 118547.
26 R. F. Pachler, K. Mayer, S. Penthor, M. Kollerits and H. Hofbauer, *International Journal of Greenhouse Gas Control*, 2018, **71**, 86-94.
27 Y. Li, Z. Li and N. Cai, *Energy & Fuels*, 2020, **34**, 11186-11193.
28 C. L. Muhich, S. Blaser, M. C. Hoes and A. Steinfeld, *Int. J. Hydrogen Energy*, 2018, **43**, 18814-18831.
29 A. J. Carrillo, K. J. Kim, Z. D. Hood, A. H. Bork and J. L. Rupp, *ACS Applied Energy Materials*, 2020, **3**, 4569-4579.
30 A. J. Carrillo, A. H. Bork, T. Moser, E. Sediva, Z. D. Hood and J. L. Rupp, *Advanced Energy Materials*, 2019, **9**, 1803886.
31 L. Qin, Y.-Y. Chen, M. Guo, Y. Liu, J. A. Fan and L.-S. Fan, *ChemCatChem*, 2021, **13**, 617-626.
32 Y. De Vos, M. Jacobs, P. Van Der Voort, I. Van Driessche, F. Snijkers and A. Verberckmoes, *Catalysts*, 2020, **10**, 926.
33 X. Zhu, K. Li, L. Neal and F. Li, *Acs Catalysis*, 2018, **8**, 8213-8236.
34 Y. Gao, X. Wang, J. Liu, C. Huang, K. Zhao, Z. Zhao, X. Wang and F. Li, *Science Advances*, 2020, **6**, eaaz9339.
35 X. Zhu, Y. Gao, X. Wang, V. Haribal, J. Liu, L. M. Neal, Z. Bao, Z. Wu, H. Wang and F. Li, *Nature communications*, 2021, **12**, 1-11.
36 K. Shah, B. Moghtaderi and T. Wall, *Energy & fuels*, 2012, **26**, 2038-2045.
37 M. Jafarian, M. Arjomandi and G. J. Nathan, *Chem. Eng. Res. Des.*, 2017, **120**, 69-81.
38 E. Krzystowczyk, X. Wang, J. Dou, V. Haribal and F. Li, *Phys. Chem. Chem. Phys.*, 2020, **22**, 8924-8932.
39 X. Wang, E. Krzystowczyk, J. Dou and F. Li, *Chem. Mater.*, 2021, **33**, 2446-2456.
40 X. Liu, R. Hong, C. Tian, *J. Mater. Sci. Mater. Electron.* 2009, **20**, 323-327.
41 Y. Feng, N. Wang and X. Guo, *Fuel*, 2019, **236**, 1057-1064.
42 J. Vieten, B. Bulfin, P. Huck, M. Horton, D. Guban, L. Zhu, Y. Lu, K. A. Persson, M. Roeb and C. Sattler, *Energy Environ. Sci.*, 2019, **12**, 1369-1384.
43 R. Michalsky and A. Steinfeld, *Catal. Today*, 2017, **286**, 124-130.
44 N. R. Singstock, C. J. Bartel, A. M. Holder and C. B. Musgrave, *Advanced Energy Materials*, 2020, **10**, 2000685.
45 A. A. Emery, J. E. Saal, S. Kirklin, V. I. Hegde and C. Wolverton, *Chem. Mater.*, 2016, **28**, 5621-5634.
46 B. W. Chen, L. Xu and M. Mavrikakis, *Chem. Rev.*, 2020, **121**, 1007-1048.
47 J. Schmidt, M. R. Marques, S. Botti and M. A. Marques, *npj Computational Materials*, 2019, **5**, 1-36.
48 K. T. Butler, D. W. Davies, H. Cartwright, O. Isayev and A. Walsh, *Nature*, 2018, **559**, 547-555.
49 S. M. Moosavi, K. M. Jablonka and B. Smit, *J. Am. Chem. Soc.*, 2020, **142**, 20273-20287.
50 F. Häse, L. M. Roch, P. Friederich and A. Aspuru-Guzik, *Nature Communications*, 2020, **11**, 1-11.
51 X. Wang, S. Ye, W. Hu, E. Sharman, R. Liu, Y. Liu, Y. Luo and J. Jiang, *J. Am. Chem. Soc.*, 2020, **142**, 7737-7743.
52 Y. Yan, T. Mattisson, P. Moldenhauer, E. J. Anthony, and P. T. Clough, *Chem. Eng. J.*, 2020, **387**, 124072.
53 J. Dou, E. Krzystowczyk, X. Wang, T. Robbins, L. Ma, X. Liu and F. Li, *ChemSusChem*, 2020, **13**, 385-393.
54 E. Marek, W. Hu, M. Gaultois, C. P. Grey and S. A. Scott, *Applied Energy*, 2018, **223**, 369-382.
55 G. Luongo, F. Donat and C. R. Müller, *Phys. Chem. Chem. Phys.*, 2020, **22**, 9272-9282.
56 T. Takeda, Y. Yamaguchi and H. Watanabe, *J. Phys. Soc. Jpn.*, 1972, **33**, 967-969.
57 Y. Wang, J. Chen and X. Wu, *Mater. Lett.*, 2001, **49**, 361-364.
58 T. Das, J. D. Nicholas and Y. Qi, *Journal of Materials Chemistry A*, 2017, **5**, 4493-4506.
59 P. Moldenhauer, P. Hallberg, M. Biermann, F. Snijkers, K. Albertsen, T. Mattisson and A. Lyngfelt, *Energy Technology*, 2020, **8**, 2000069.
60 M. Arjmand, R. F. Kooiman, M. Rydén, H. Leion, T. Mattisson and A. Lyngfelt, *Energy & fuels*, 2014, **28**, 1312-1324.
61 A. Cabello, A. Abad, P. Gayán, F. García-Labiano, F. Luis and J. Adánez, *Applied Energy*, 2021, **287**, 116557.
62 D. Maiti, B. J. Hare, Y. A. Daza, A. E. Ramos, J. N. Kuhn and V. R. Bhethanabotla, *Energy Environ. Sci.*, 2018, **11**, 648-659.
63 J. Zhang, V. Haribal and F. Li, *Science advances*, 2017, **3**, e1701184.
64 D. D. Taylor, N. J. Schreiber, B. D. Levitas, W. Xu, P. S. Whitfield and E. E. Rodriguez, *Chem. Mater.*, 2016, **28**, 3951-3960.
65 N. Miura, H. Ikeda and A. Tsuchida, *Industrial & Engineering Chemistry Research*, 2016, **55**, 3091-3096.
66 J. Vieten, B. Bulfin, F. Call, M. Lange, M. Schmücker, A. Francke, M. Roeb and C. Sattler, *Journal of Materials Chemistry A*, 2016, **4**, 13652-13659.
67 J. Vieten, B. Bulfin, M. Senholdt, M. Roeb, C. Sattler and M. Schmücker, *Solid State Ionics*, 2017, **308**, 149-155.
68 Z. Yang, Y. Lin and Y. Zeng, *Industrial & engineering chemistry research*, 2002, **41**, 2775-2784.
69 Z. Yang and Y. Lin, *Industrial & engineering chemistry research*, 2003, **42**, 4376-4381.
70 J. Dou, E. Krzystowczyk, X. Wang, A. R. Richard, T. Robbins and F. Li, *Journal of Physics: Energy*, 2020, **2**, 025007.
71 R. Banerjee, S. Chatterjee, M. Ranjan, T. Bhattacharya, S.

Mukherjee, S. S. Jana, A. Dwivedi and T. Maiti, *ACS Sustainable Chemistry & Engineering*, 2020, **8**, 17022-17032.
72 L. Buitinck, G. Louppe, M. Blondel, F. Pedregosa, A. Mueller, O. Grisel, V. Niculae, P. Prettenhofer, A. Gramfort, J. Grobler, and R. Layton, 2013, arXiv preprint arXiv, 1309.0238.
73 C. J. Bartel, C. Sutton, B. R. Goldsmith, R. Ouyang, C. B. Musgrave, L. M. Ghiringhelli and M. Scheffler, *Sci. Adv.*, 2019, **5**, eaav0693.
74 D. Maiti, Y. A. Daza, M. M. Yung, J. N. Kuhn and V. R. Bhethanabotla, *Journal of Materials Chemistry A*, 2016, **4**, 5137-5148.
75 V. P. Haribal, F. He, A. Mishra and F. Li, *ChemSusChem*, 2017, **10**, 3402-3408.
76 G. Pasha and M. Shah, *Journal of research (Science)*, 2004, **15**, 97-106.
77 J. Ranstam and J. Cook, *Journal of British Surgery*, 2018, **105**, 1348-1348.
78 C. Campbell and Y. Ying, *Synthesis lectures on artificial intelligence and machine learning*, 2011, **5**, 1-95.
79 O. Kramer, *Dimensionality reduction with unsupervised nearest neighbors*, Springer, 2013.
80 C. K. Williams and C. E. Rasmussen, *Gaussian processes for machine learning*, MIT press Cambridge, MA, 2006.
81 J. Simm, I. M. De Abril and M. Sugiyama, *IEICE TRANSACTIONS on Information and Systems*, 2014, **97**, 1677-1681.
82 L. Breiman, *Machine Learning*, 2001, **45**, 5-32.
83 G. Panapitiya, G. Avendaño-Franco, P. Ren, X. Wen, Y. Li and J. P. Lewis, *J. Am. Chem. Soc.*, 2018, **140**, 17508-17514.
84 S. B. Torrisi, M. R. Carbone, B. A. Rohr, J. H. Montoya, Y. Ha, J. Yano, S. K. Suram and L. Hung, *NPJ Comput. Mater.* 2020, **6**, 1-11.
85 B. Huang, and O. A. V. Lilienfeld, *Chem. Rev.*, 2021, **121**, 10001-10036.
86 H. Wei, S. Ye, Y. Zhang, T. Li, G. Zhang, Y. Luo, S. Mukamel and J. Jiang, *J. Phys. Chem. Lett.*, 2019, **10**, 6026-6031.
87 Y. Shi, N. Ni, Q. Ding, X. Zhao, *J. Mater. Chem. A*, 2022, **10**, 2256-2270.
88 L. Tang, Z. Li, K. Chen, C. Li, X. Zhang and L. An, *J. Am. Ceram. Soc.*, 2021, **104**, 1953-1958.
89 S. Jiang, T. Hu, J. Gild, N. Zhou, J. Nie, M. Qin, T. Harrington, K. Vecchio and J. Luo, *Scr. Mater.*, 2018, **142**, 116-120.
90 https://github.com/xwsci/High_throughput_screening_Perovskites_for_CL
91 N. Miura, H. Ikeda and A. Tsuchida, *Industrial & Engineering Chemistry Research*, 2016, **55**, 3091-3096.
92 V. Josua, B. Brendan, D. E. Starr, H. Atsushi, G. De, A. Anahita, Z. Carolin, H. Michael, S. Katarzyna and K. Nicole, *Energy Technology*, 2018.
93 E. Krzystowczyk, X. Wang, J. Dou, V. Haribal and F. Li, *Phys. Chem. Chem. Phys.*, 2020, **22**.
94 R. H. Grke, E. J. Marek, F. Donat and S. A. Scott, *International Journal of Greenhouse Gas Control*, 2020, **94**, 102891.
95 J. Dou, E. Krzystowczyk, X. Wang, A. R. Richard and F. Li, *Journal of Physics Energy*, 2020, **2**.
96 J. F. Vente, S. Mcintosh, W. G. Haije and H. Bouwmeester, *J. Solid State Electrochem.*, 2006, **10**, 581-588.
97 J. Vieten, B. Bulfin, F. Call, M. Lange, M. Schmücker, A. Francke, M. Roeb and C. Sattler, *J. Mater. Chem. A*, 2016, **35**, 13652-13659.
98 H. C. Wu and Y. S. Lin, *Ind. Eng. Chem. Res.*, 2017, **56**, 6057-6064.
99 D. Jian, E. Krzystowczyk, A. Mishra, X. Liu and F. Li, *ACS Sustainable Chemistry And Engineering*, 2018, **6**, 15528-15540.
100 F. He, J. Chen, S. Liu, Z. Huang, G. Wei, G. Wang, Y. Cao and K. Zhao, *Int. J. Hydrogen Energy*, 2019, **44**, 10265-10276.
101 K. Zhao, F. He, Z. Huang, G. Wei, A. Zheng, H. Li and Z. Zhao, *Applied Energy*, 2016, **168**, 193-203.
102 K. Zhao, F. He, Z. Huang, G. Wei, A. Zheng, H. Li and Z. Zhao, *Korean J. Chem. Eng.*, 2017, **34**, 1651-1660.
103 K. Zhao, H. Fang, Z. Huang, A. Zheng and Z. Zhao, *Int. J. Hydrogen Energy*, 2014, **39**, 3243–3252.
104 Y. Shen, K. Zhao, F. He and H. Li, *Journal of the Energy Institute*, 2019, **92**, 239-246.
105 Q. Jiang, Y. Gao, V. P. Haribal, H. Qi and F. Li, *Journal of Materials Chemistry A*, 2020, **8**, 13173-13182.
106 S. Iftikhar, Q. Jiang, Y. Gao, J. Liu, H. Gu, L. Neal and F. Li, *Energy Fuels*, 2021, **35**, 13921-13929.
107 L. Nalbandian, A. Evdou and V. Zaspalis, *Int. J. Hydrogen Energy*, 2011, **36**, 6657-6670.
108 A. Shafiefarhood, J. Zhang, L. M. Neal and F. Li, *J. Mater. Chem. A*, 2017, **5**, 11930–11939
109 W. Gao, J. Guo, P. Wang, F. Chang, Q. Pei, W. Zhang, L. Liu and P. Chen, *Nat. Energy*, 2018,**3**, 1067-1075.
110 A. J. Carrillo, K. J. Kim, Z. D. Hood, A. H. Bork and J. L. M. Rupp, *ACS Appl. Energy Mater.*, 2020, **3**, 4569-4579.
111 Q. Jiang, Y. Gao, V. P. Haribal, H. Qi, X. Liu, H. Hong, H. Jin and F. Li, *J. Mater. Chem. A*, 2020, **8**, 13173-13182.
112 G. G. Kresse and J. J. Furthmüller, *Physical review. B, Condensed matter*, 1996, **54**, 11169.
113 P. Blöchl, *Physical review. B, Condensed matter*, 1994, **50**, 17953.
114 J. Perdew, K. Burke and M. Ernzerhof, *Phys. Rev. Lett.*, 1997, **77**, 3865.
115 V. I. Anisimov, J. Zaanen and O. K. Andersen, *Physical review. B, Condensed matter*, 1991, **44**, 943-954.
116 A. Jain, G. Hautier, C. J. Moore, S. P. Ong, C. C. Fischer, T. Mueller, K. A. Persson and G. Ceder, *Computational Materials Science*, 2011, **50**, 2295-2310.
117 G. Hautier, S. P. Ong, A. Jain, C. J. Moore and G. Ceder, *Physical review. B, Condensed matter*, 2011, **85**, 155208.
118 Y. L. Lee, J. Kleis, J. Rossmeisl and D. Morgan, *Physical Review B*, 2009, **80**, 308-310.
119 A. V. D. Walle, P. Tiwary, M. De Jong, D. L. Olmsted, M. Asta, A. Dick, D. Shin, Y. Wang, L. Q. Chen and Z. K. Liu, *Calphad-computer Coupling of Phase Diagrams & Thermochemistry*, 2013, **42**, 13-18.
120 A. Togo and I. Tanaka, *Scripta Mater.*, 2015, **108**, 1-5.
121 B. Bulfin, J. Vieten, D. E. Starr, A. Azarpira, C. Zachäus, M. Hävecker, K. Skorupska, M. Schmücker, M. Roeb and C. Sattler, *J. Mater. Chem. A*, 2017, **5**, 7912-7919.
122 R. P. Stoffel, C. Wessel, M. W. Lumey, R. Dronskowski, *Angew. Chem. Int. Ed.* 2010, **49**, 5242–5266.
123 A. J. Jackson, A. Walsh, *J. Mater. Chem. A*, 2014, **2**, 7829-7836.
124 Frisch, M. J.; Trucks, G. W.; Schlegel, H. B.; Scuseria, G. E.; Robb, M. A.; Cheeseman, J. R.; Scalmani, G.; Barone, V.; Petersson, G. A.; Nakatsuji, H.. et al.Gaussian 16, revision C. 01; Gaussian Inc.: Wallingford, CT, USA., 2016.
125 A. Abraham, F. Pedregosa, M. Eickenberg, P. Gervais, A. Muller, J. Kossaifi, A. Gramfort, B. Thirion and G. Varoquaux, 2014, **8**, 14.